Final Draft

of the original manuscript

Bazazzadeh, S.; Mossaiby, F.; Shojaei, A.:

An adaptive thermo-mechanical peridynamic model for fracture analysis in ceramics.

In: Engineering Fracture Mechanics. Vol. 223 (2020) 106708.
First published online by Elsevier: 17.10.2019

https://dx.doi.org/10.1016/j.engfracmech.2019.106708

An adaptive thermo-mechanical peridynamic model for fracture analysis in ceramics

Soheil Bazazzadeh[a,b,*], Farshid Mossaiby[c], Arman Shojaei[d]

[a]*Industrial Engineering Department, University of Padova, v. Venezia 1, Padova 35131, Italy*
[b]*Center of Studies and Activities for Space (CISAS)-"G. Colombo", v. Venezia 15, Padova 35131, Italy*
[c]*Department of Civil Engineering, University of Isfahan, 81744-73441 Isfahan, Iran*
[d]*Institute of Materials Research, Materials Mechanics, Helmholtz-Zentrum Geesthacht, Max-Planck-Strasse 1, 21502, Geesthacht, Germany*

Abstract

A thermo-mechanical peridynamic model using adaptive grid refinement is developed to investigate crack propagation in ceramics. Compared to a standard peridynamic model, using uniform grid, this approach allows to increase the resolution of analysis only in the critical zones. The performance of this approach in solving 2D thermo-elastic problems is examined and then it is applied to study the fracture of a ceramic disk under central thermal shock. Finally, the proposed approach is adopted to investigate thermal shock in thin rectangular and circular slabs. The accuracy of the method is evaluated by comparing its numerical results with those obtained by applying the finite element method (FEM), a standard peridynamic approach or with experimental data available in the literature. A proper agreement is achieved at a smaller computational cost.

Keywords: Peridynamics, thermal shock, adaptive grid refinement, ceramics, thermo-mechanical

1. Introduction

Thermal shock is a phenomenon characterized by significant inhomogeneous stresses suddenly occurring in brittle materials, such as ceramics, due to a transient temperature. Complex crack patterns may emerge on ceramics as a crucial outcome of thermal shock

*Corresponding author
Email address: soheil.bazazzadeh@phd.unipd.it (Soheil Bazazzadeh)

induced stresses. Ceramics have a wide range of applications in high-temperature industries such as aircraft propulsion, hypersonic vehicles, marine propulsion and thermal protection structures due to their stability above the melting point of metal alloys. Hence, a basic understanding of thermal shock failure is required in the design of the aforementioned structures [1].

Numerous experimental and numerical studies have been performed over the last few decades to investigate the mechanisms of thermal shock failure in ceramics. Among the experimental studies, Jiang et al [2] and Shao et al [3] have studied thermal shock in thin rectangular ceramic specimens, while in the studies by Honda and Liu [4–6] the thermal shock in circular ceramic specimens is explored comprehensively. Thermal shock cracks generally exhibit periodic and hierarchical damage patterns. In the studies by [7, 8], the length and stability of the crack patterns have been scrutinized theoretically. Among the theoretical studies, thermal shock resistance has been investigated from the viewpoint of stress and energy [9, 10]. Later, thermal shock parameters related to the fracture initiation, crack propagation and crack arrest criteria of ceramic specimens were investigated in [11, 12].

However, available computational techniques based on the classical theory of continuum mechanics cannot accurately describe how complex crack patterns nucleate and evolve. To this end, several researchers have introduced a wide range of computational techniques to solve the problem and equipped computational methods based on the classical theory with the capability to precisely describe crack propagation phenomena. Among the numerical methods, the boundary element method (BEM) was used to simulate quenching thermal shock [13, 14]. Later, the extended finite element method (XFEM) with nodal enrichment [15–17], the phase field method [18, 19], damage mechanics-based model [20] and nonlocal damage model [21] have been applied to reproduce the multiple cracking patterns in the quenching test with different levels of success. The majority of these techniques make use of *ad-hoc* modifications and simplifying assumptions. Furthermore, their application to 3D problems generally turns out to be very complex.

Peridynamics is a nonlocal theory which was first proposed by Silling *et al.* [22, 23]. Peridynamics makes description of discontinuous problems in solid mechanics

very convenient. It employs integral equations rather than partial differential equations (PDEs) to determine the internal forces over the continuum. Applications of peridynamics to solve various problems with discontinuity can be traced in [24–28]. In [29, 30], single and multiple pre-existing initial cracks due to prescribed thermal temperature history (without applying any thermo-mechanical coupling) are simulated using the peridynamic approach. Furthermore, the peridynamics formulation was developed for multiphysics problem; e.g. thermal diffusion in [31]. Soon afterwards, heat transfer equations for 1D and 2D problems were reformulated in [32] and [33], respectively. Moreover, Oterkus *et al.* [34] carried out a detailed investigation of thermal diffusion problems by using state-based peridynamics (SB-PD).

Agwai and Oterkus *et al.* investigated thermo-elastic problems without any crack propagations via peridynamic [35, 36]. Lately, thermal cracking of uranium dioxide in fuel pellets and simulation of thermal shock cracking in ceramics using a bond-based peridynamic model (BB-PD) have been thoroughly explored in [37]. Furthermore, in [38], 2D and 3D thermal-shocks of ceramic slabs are simulated using a SB-PD model. Other applications of peridynamics to simulate thermal shock crack propagation in brittle materials, e.g. rocks, can be traced in [39–42].

It is remarkable that the conventional peridynamic models are computationally more expensive than the methods based on the classical theories due to their nonlocal nature. Moreover, in a conventional peridynamic approach, a constant horizon size as well as a uniform grid are used. Therefore, the efficiency of the approach is strongly affected when a fine grid spacing is adopted; although the finest grid size would be usually needed only in specific zones [43]. There have been many attempts so far to maintain the computational accuracy and to reduce, at the same time, the computational cost of peridynamic models. Possible ways to achieve that is to couple peridynamic models with other methods [44–47], to use adaptive refinement algorithms [30, 43, 48, 49], or benefiting from parallel computing techniques [50].

The main purpose of the present study is the solution of thermal shock problems in ceramics, including crack propagation, using a multi-grid peridynamic model. The model is originally introduced in [49] for dynamic propagation of cracks merely under mechanical loading conditions. The method adaptively makes use of a variable grid

size at different parts of the solution domain. The problem domain, Ω, is divided in two regions Ω^+ (coarse) and Ω^- (fine), where two different grid spacing are used. By applying the fine grid size near the boundaries of the domain, one is able to reduce the surface effect and consequently to increase the accuracy of the peridynamic model. The adaptive grid refinement model proposed in [49] offers some advantages, in terms of accuracy and efficiency, which can be highly important for the coupled thermo-mechanical problems conducted in the present study. In fact, the model proposed by the authors in [49], exhibits highly accurate results, with respect to a standard peridynamic model discretized using a uniform grid of nodes, not only at the level of displacement but also at the level of velocity and acceleration. In addition, the multi-grid model has a negligible loss of volume due to non-uniform discretization in comparison to other available grid refinement approaches in the literature. These features culminates in a robust model that performs properly even in situations where intensive propagating waves and, consequently, nucleation and propagation of cracks with complex patterns occur. Such situations can be abundantly found in the case of thermal-shock (quenching).

The aforementioned advantages of the multi-grid model in [49] led us to apply that for thermo-mechanical problems including cracks. Basically, for this class of problems most often, to capture a converged solution with a proper level of accuracy, a very fine discretization in space and time for the whole problem domain of a standard peridynamic model is required. Therefore, application of a standard peridynamic model to such cases turns out to be computationally very prohibitive. We shall show that the multi-grid model developed in the present study can be a good candidate to alleviate these shortcomings of the standard peridynamic model. By the present model, it is possible to increase the resolution of the solution at critical parts, which require a fine discretization, adaptively. This strategy contributes to a significant reduction in the computational cost. Another important aspect of the present paper is the use of an adaptive refinement technique in both thermal and mechanical parts of the solution. Comparing the results of the proposed method to those generated by standard peridynamic models, reveals that one can obtain very similar results at a smaller computational cost. This method produces accurate results in both temperature and displacement fields.

The outline of the paper is as follows. Section 2 provides an overview of weakly

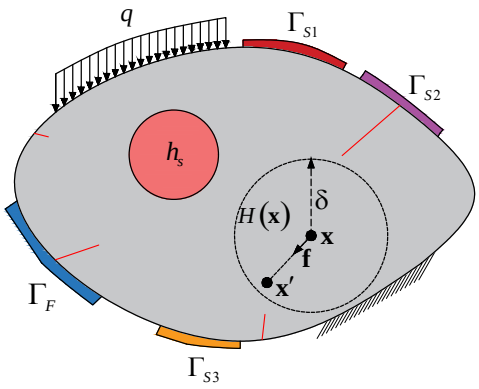

Figure 1: A generic problem domain and representation of horizon, source and neighboring material points in peridynamics.

coupled thermo-mechanics and its discretization. The mathematical description of the coupling between different grids is illustrated in Section 3, while in Section 4, we explain an efficient way to implement the adaptive refinement technique. Efficiency and accuracy of the method are investigated by several examples in Section 5. Section 6 concludes the paper.

2. Overview of weakly coupled thermo-mechanical peridynamics

2.1. Thermal problem

The application of a SB-PD model to heat conduction problems was firstly introduced by Oterkus *et al.* [34]. The nonlocal interaction between material points, for thermal diffusion problems using the peridynamic framework, is related to the exchange of heat flux. Hence, a material point $\mathbf{x}$ (the source node) is able to exchange heat flux with the so called *family points* located within its integration domain; i.e, $\mathbf{x}' \in H(\mathbf{x})$ (see Figure 1). In this way, the transient form of the SB-PD thermal diffusion equation can be written as:

$$\rho c_v \dot{\theta}(\mathbf{x},t) = \int_{H(\mathbf{x})} \left(\underline{h}[\mathbf{x},t]\langle \mathbf{x}' - \mathbf{x} \rangle - \underline{h}[\mathbf{x}',t]\langle \mathbf{x} - \mathbf{x}' \rangle \right) dV_{\mathbf{x}'} + h_s(\mathbf{x},t) \qquad (1)$$

where $\underline{h}[\mathbf{x}, t]$ represents the heat flow scalar state and $h_s(\mathbf{x}, t)$ is the heat source due to volumetric heat generation. In fact, to each material point $\mathbf{x}$ an infinitesimal volume $dV_{\mathbf{x}}$ is allocated. In Eq. (1), ρ and c_v are the density of the material and specific heat capacity, respectively. Moreover, θ and $\dot{\theta}$ denote the temperature and its first time derivative at point $\mathbf{x}$, respectively. The relative position between two material points $\boldsymbol{\xi} = \mathbf{x} - \mathbf{x}'$ is called a *bond*. In BB-PD, it is assumed that the heat flux only takes place over a bond connecting two material points, and it depends on the temperature difference between the points. In this sense, the heat flux that flows from $\mathbf{x}'$ to $\mathbf{x}$, $\underline{h}[\mathbf{x}, t]\langle \mathbf{x}' - \mathbf{x} \rangle$, and the one which flows from $\mathbf{x}$ to $\mathbf{x}'$, $\underline{h}[\mathbf{x}', t]\langle \mathbf{x} - \mathbf{x}' \rangle$, are equal in magnitude but opposite in direction. Accordingly, in the BB-PD formulation, the heat flux towards the source point can be written as:

$$f_h\left(\theta', \theta, \mathbf{x}', \mathbf{x}\right) = \underline{h}[\mathbf{x}, t]\langle \mathbf{x}' - \mathbf{x} \rangle - \underline{h}[\mathbf{x}', t]\langle \mathbf{x} - \mathbf{x}' \rangle \equiv \frac{1}{2} f_h - \left(-\frac{1}{2} f_h\right) \tag{2}$$

Therefore, substitution of Eq. (2) for Eq. (1), leads to the following heat conduction equation:

$$\rho c_v \dot{\theta}(\mathbf{x}, t) = \int_{H(\mathbf{x})} f_h\left(\theta', \theta, \mathbf{x}', \mathbf{x}\right) dV_{\mathbf{x}'} + h_s(\mathbf{x}, t) \tag{3}$$

where f_h is given by [34]:

$$f_h\left(\theta', \theta, \mathbf{x}', \mathbf{x}\right) = c_{TH} \frac{\tau\left(\mathbf{x}', \mathbf{x}, t\right)}{\|\boldsymbol{\xi}\|} \tag{4}$$

in which $\tau\left(\mathbf{x}', \mathbf{x}, t\right)$ stands for the temperature difference between the interacting points as:

$$\tau\left(\mathbf{x}', \mathbf{x}, t\right) = \theta\left(\mathbf{x}', t\right) - \theta\left(\mathbf{x}, t\right) \tag{5}$$

In Eq. (4), c_{TH} represents the thermal micro-conductivity in peridynamics which can be expressed in terms of the standard conductivity for a specific horizon. This can be done by equating the peridynamic thermal potential to the classical thermal potential at a material point (the details are given in [33, 34]). In this way, the thermal micro-modulus c_{TH} can be found in terms of the thermal conductivity γ for 1D, 2D and 3D cases as:

$$c_{TH} = \begin{cases} \frac{2\gamma}{A\delta^2}, & \text{1D problems} \\ \frac{6\gamma}{\pi t \delta^3}, & \text{2D problems} \\ \frac{6\gamma}{\pi \delta^4}, & \text{3D problems} \end{cases} \tag{6}$$

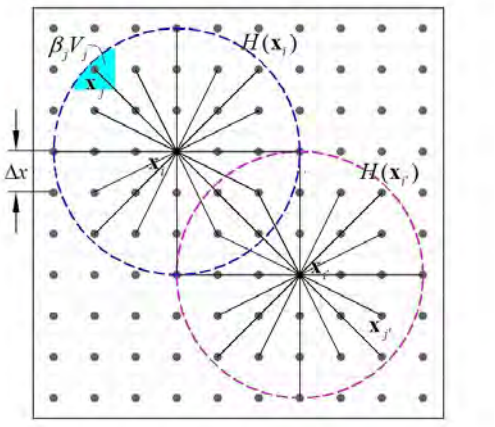

Figure 2: Peridynamic nodes and their interactions.

in which, A and $\bar{t}$ represent the cross-sectional area and thickness of the volume allocated to the material point, respectively.

The continuum formulation can be discretized in several ways [51]. In the present study, the discretization is done pursuing a meshfree approach originally introduced in [52]; the discretization is simple to implement and it is commonly applied by many researchers (see Figure 2). In 2D problems, which is the case for the present study, the domain is represented by a grid of points; hereinafter are called nodes. To each node a square cell, with a volume equal to $\Delta x^2 \bar{t}$, is allocated. The cells are centered at their corresponding nodes. As shown in Figure 2, each node $\mathbf{x}_i$ interacts with all the nodes within its horizon; we refer to $\mathbf{x}_i$ and $\mathbf{x}_j$ as the source node and the family node, respectively. The horizon size is taken equal to $\delta = m\Delta x$. The value of m determines the number of interacting nodes. In the conventional discretization, Δx, δ and m are taken constant in the whole domain. Furthermore, time can be discretized into instants as $t_1, t_2, \ldots, t_n, \ldots$. In this way, by adopting the one-point Gauss quadrature rule for the integration in space, the discretized form of Eq. (3) can be written as:

$$\rho c_v \dot{\theta}_i^n = \sum_{j=1}^{N} f_h \left(\tau^n (\mathbf{x}_j - \mathbf{x}_i) \right) V_j + h_{s(i)}^n \tag{7}$$

where N stands for the total number of family nodes and V_j represents the volume of node $\mathbf{x}_j$. To proceed in time, various time integration schemes can be applied. In this

study, a forward difference time marching is employed; therefore, having known the field variable at time instant t_n, the solver can advance to the next time step as follows:

$$\theta_i^{n+1} = \theta_i^n + \frac{\Delta t_{TH}}{\rho c_v} \left[\sum_{j=1}^{N} f_h \left(\tau^n (\mathbf{x}_j - \mathbf{x}_i) \right) V_j + h_{s(i)}^n \right] \tag{8}$$

where, Δt_{TH} is the incremental time step corresponding to the thermal analysis and $h_{s(i)}^n = h(\mathbf{x}_i, t_n)$. Δt_{TH} must be selected within a proper range to achieve a stable solution. The upper bound of the range can be expressed as [34, 52]:

$$\Delta t_{TH} < \frac{\rho c_v}{\sum_{j=1}^{N} \frac{c_{TH}}{\|\xi\|} V_j} \tag{9}$$

2.1.1. Boundary conditions

Thermal diffusion boundary conditions, which are Dirichlet-type, should be imposed on corresponding boundary surfaces denoted by Γ_F. For this type of conditions, it just suffices to assign a temperature to each node located within a distance Δx close to Γ_F (Figure 1). On the other hand, Neumann-type boundary conditions appear in the form of heat flux, convection, and radiation.

To apply heat flux boundary conditions, at first the rate of heat entering into the body from the bounding surface must be calculated. Then the rate of flowing heat $\dot{Q}$ must be converted to a volumetric value $\tilde{Q}$; called heat generation per unit volume. In this way, the heat flux portion of each node, on the corresponding boundary region, can be specified. By assuming an identical cross-sectional area for the nodes we have:

$$\tilde{Q} = \frac{\dot{Q}}{V_f} = -\frac{\int_S \mathbf{q} \cdot \mathbf{n} dS}{S \Delta x} = -\frac{\mathbf{q} \cdot \mathbf{n}}{\Delta x} \tag{10}$$

where $\mathbf{q}$ is the heat flux, S is the area to which the heat flux is imposed (i.e, the surface area of Γ_{S1} shown in Figure 1), and V_f is the volume of the boundary region.

The convection boundary condition (Neumann), for example in the case of a quenching test where heat transfer between the surface of a body and its surrounding takes place, is defined as:

$$\mathbf{q}(\mathbf{x}, t) \cdot \mathbf{n} = h \left(\theta(\mathbf{x}, t) - \theta_\infty \right), \quad \mathbf{x} \in \Gamma_{S2} \tag{11}$$

where, h is the convective heat transfer coefficient, θ_∞ is the temperature of the fluid surrounding the domain (see Figure 1). Consequently, similar to Eq. (10), volumetric heat generation due to the convection boundary condition is given by:

$$h_s(\mathbf{x},t) = \frac{1}{\Delta x} h \left(\theta_\infty - \theta(\mathbf{x},t)\right), \quad \mathbf{x} \in \Gamma_{S2} \tag{12}$$

The third Neumann-type boundary condition is radiation. Similarly, heat generation per unit volume for radiation heat transfer is assigned to the nodes located at Γ_{S3} (see Figure 1) as:

$$h_s = \frac{1}{\Delta x} \epsilon\sigma \left(\theta_{ss}^4 - \theta^4(\mathbf{x},t)\right), \quad \mathbf{x} \in \Gamma_{S3} \tag{13}$$

where σ, ϵ and θ_{ss} are the Stefan-Boltzmann constant, emissivity of the surface and temperature of the surface surrounding the body, respectively.

In the subsequent section, the strategy to cope with the mechanical part of solution, using peridynamics having a similar discretization scheme in space, is illustrated. Then the way of incorporating the thermal effects into the mechanical solution is described.

2.2. Mechanical problem

Let us consider again a body, with an initial configuration Ω, occupying a 3D region in space (see Figure 3). Based on SB-PD, the equation of motion is written by:

$$\rho(\mathbf{x}) \frac{\partial^2 \mathbf{u}}{\partial t^2}(\mathbf{x},t) = \int_{H(\mathbf{x})} \left(\underline{\mathbf{T}}[\mathbf{x},t]\langle \mathbf{x}' - \mathbf{x}\rangle - \underline{\mathbf{T}}[\mathbf{x}',t]\langle \mathbf{x} - \mathbf{x}'\rangle\right) dV_{\mathbf{x}'} + \mathbf{b}(\mathbf{x},t) \tag{14}$$

where $\underline{\mathbf{T}}$ stands for the force vector state, which the material point $\mathbf{x}'$ exerts on material point $\mathbf{x}$. In Eq. (14), similar to the thermal diffusion problem, two material points interact only within a finite distance, δ. Moreover, ρ, $\mathbf{u}$ and $\mathbf{b}$ are the mass density, displacement field and body force density, respectively. According to the linearized formulation proposed in [23], the force vector state $\underline{\mathbf{T}}$ is given by:

$$\underline{\mathbf{T}}[\mathbf{x},t]\langle \mathbf{x}' - \mathbf{x}\rangle = \left(\frac{3k\bar{\theta}}{m}\underline{\omega x} + \frac{15\mu'}{m}\underline{\omega e^d}\right) \frac{\underline{\mathbf{Y}}[\mathbf{x},t]\langle \mathbf{x}' - \mathbf{x}\rangle}{\|\underline{\mathbf{Y}}[\mathbf{x},t]\langle \mathbf{x}' - \mathbf{x}\rangle\|} \tag{15}$$

in which k and μ' are the material parameters related to Young's modulus E and Poisson's ratio ν, while the position of point $\mathbf{x}$ at time t is denoted by $\mathbf{y}(\mathbf{x},t) = \mathbf{x} + \mathbf{u}(\mathbf{x},t)$.

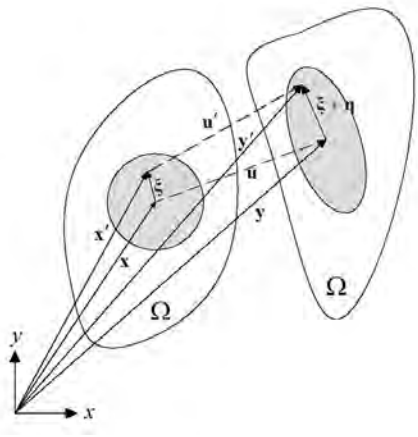

Figure 3: Kinematics of the reference and deformed configurations for a peridynamic continuum.

Therefore, one may obtain the deformation vector state, $\underline{\mathbf{Y}}[\mathbf{x}, t]\langle \mathbf{x}' - \mathbf{x} \rangle$, and extension scalar state, $\underline{e}[\mathbf{x}, t]\langle \boldsymbol{\xi} \rangle$, as:

$$\underline{\mathbf{Y}}[\mathbf{x}, t]\langle \mathbf{x}' - \mathbf{x} \rangle = \mathbf{y}(\mathbf{x}', t) - \mathbf{y}(\mathbf{x}, t) \tag{16}$$

$$\underline{e}[\mathbf{x}, t]\langle \boldsymbol{\xi} \rangle = \|\mathbf{y}(\mathbf{x}', t) - \mathbf{y}(\mathbf{x}, t)\| - \|\boldsymbol{\xi}\| \tag{17}$$

where the relative displacement vector between two points is defined as $\boldsymbol{\eta} = \mathbf{u}' - \mathbf{u}$. Moreover, the deviatoric state component of the single bond elongation $\underline{e}$ is given by:

$$\underline{e}^d = \underline{e} - \frac{\bar{\theta}}{3}\underline{x} \tag{18}$$

In Eq. (15), $\underline{\omega}$ is a scalar influence function that allocates a weight to each bond. The peridynamics counterpart of volume dilatation $\Delta V / V$ can be expressed by:

$$\bar{\theta} = \frac{3}{m}\underline{\omega x} \bullet \underline{e} = \frac{3}{m}\int_{H(\mathbf{x})} \omega \bar{s} \|\boldsymbol{\xi}\|^2 d\xi \tag{19}$$

where the weighted volume, m, is given by:

$$m = \underline{\omega x} \bullet \underline{e} = \int_{H(\mathbf{x})} \omega \|\boldsymbol{\xi}\|^2 d\xi \tag{20}$$

and the total stretch in each bond can be written as:

$$\bar{s} = s - \alpha T_{avg} \tag{21}$$

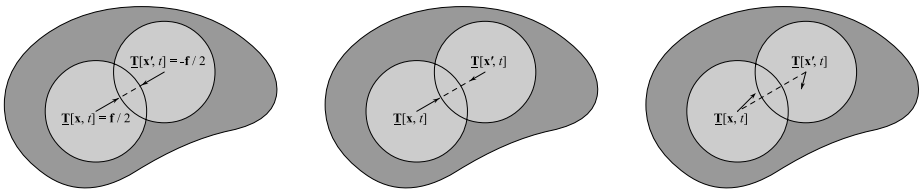

Figure 4: The force density schemes in (a) BB-PD (b) OSB-PD (c) NOSB-PD.

in which, α is the thermal expansion coefficient and T_{avg} is defined by:

$$T_{avg} = \frac{(\theta - \theta_0) + (\theta' - \theta_0)}{2} \tag{22}$$

where, θ_0 represents the reference temperature, θ and θ' indicate the temperature at material points $\mathbf{x}$ and $\mathbf{x}'$, respectively. Moreover, s, in Eq. (21), denotes the relative elongation (stretch) of the bond, defined by [22]:

$$s = \frac{\|\boldsymbol{\xi} + \boldsymbol{\eta}\| - \|\boldsymbol{\xi}\|}{\|\boldsymbol{\xi}\|} \tag{23}$$

In ordinary state based peridynamics (OSB-PD) pairwise force states are not equal ($\underline{\mathbf{T}}[\mathbf{x}', t]\langle \mathbf{x}' - \mathbf{x} \rangle \neq -\underline{\mathbf{T}}[\mathbf{x}, t]\langle \mathbf{x} - \mathbf{x}' \rangle$) although they are co-axial (see Figure 4b); in non-ordinary state based peridynamics (NOSB-PD), pairwise force states are neither equal nor co-axial (see Figure 4c). On the other hand, in BB-PD the interaction between two material points is totally independent of other bonds. Hence, the force state that two points exert on each other are equal in magnitude but opposite in sign ($\underline{\mathbf{T}}[\mathbf{x}', t]\langle \mathbf{x}' - \mathbf{x} \rangle = -\underline{\mathbf{T}}[\mathbf{x}, t]\langle \mathbf{x} - \mathbf{x}' \rangle$) (see Figure 4a). Therefore, Eq. (14) can be simplified for BB-PD and takes the following form:

$$\rho(\mathbf{x})\ddot{\mathbf{u}}(\mathbf{x}, t) = \int_{H(\mathbf{x})} \mathbf{f}\left(\mathbf{u}(\mathbf{x}', t) - \mathbf{u}(\mathbf{x}, t), \mathbf{x}' - \mathbf{x}\right) dV_{x'} + \mathbf{b}(\mathbf{x}, t) \tag{24}$$

in which $\mathbf{f}$ is the pairwise force function of each bond, respectively.

In fact, in BB-PD the bond force only depends on two interacting material points within a continuum; hence, this formulation is restricted to a fixed value of Poisson's ratio. This value for 3D and plane strain cases is $\nu = 1/4$ and for plane stress cases is $\nu = 1/3$. By using the prototype microelastic brittle (PMB) model [52], with a

constitutive law depicted in Figure 5, one may obtain the pairwise force function as:

$$\mathbf{f}\left(\mathbf{u}'-\mathbf{u},\mathbf{x}'-\mathbf{x},t\right)=\mu(\xi,t)c_{ME}\omega(\xi)\left(s-\alpha T_{avg}\right)\frac{\mathbf{y}(\mathbf{x}',t)-\mathbf{y}(\mathbf{x},t)}{\|\mathbf{y}(\mathbf{x}',t)-\mathbf{y}(\mathbf{x},t)\|} \tag{25}$$

in which c_{ME} is the micro-modulus that can be interpreted as the bond stiffness. $\mu(\xi,t)$ is a history-dependent function which takes the value of 1 for active bonds and 0 for broken bonds. ω is known as the degree of interactions between points. Considering the elastic deformation energy, one can define the mechanical micro-modulus in terms of the Young's modulus E and of the horizon radius δ as:

$$c_{ME}=\begin{cases}\frac{9E}{\pi t_h\delta^3}, & \text{Plane stress}\\ \frac{48E}{5\pi t_h\delta^3}, & \text{Plane strain}\\ \frac{12E}{\pi\delta^4}, & \text{3D}\end{cases} \tag{26}$$

Furthermore, it is possible to obtain critical stretch, s_0, in terms of the critical energy release rate of the material, G_0 [52, 53]:

$$s_0=\begin{cases}\sqrt{\frac{4\pi G_0}{9E\bar{t}\delta}}, & \text{Plane stress}\\ \sqrt{\frac{5\pi G_0}{12E\bar{t}\delta}}, & \text{Plane strain}\\ \sqrt{\frac{5G_0}{6E\delta}}, & \text{3D}\end{cases} \tag{27}$$

A bond is considered broken and is removed from the following calculations when:

$$s-\alpha T_{avg}\geq s_0 \tag{28}$$

The damage level of point $\mathbf{x}$ at time t can be expressed by:

$$\phi(\mathbf{x},t)=1-\frac{\int_{H(\mathbf{x})}\mu(\boldsymbol{\xi},t)dV_{\mathbf{x}'}}{\int_{H(\mathbf{x})}dV_{\mathbf{x}'}} \tag{29}$$

In Eq. (29), ϕ indicates the ratio of the number of broken bonds to the total number of bonds originally connected to point $\mathbf{x}$ and takes a value between 0 and 1. The case $\phi=1$ means that there is no interaction between the point and all surrounding points within its horizon, while $\phi=0$ denotes an undamaged state.

Similar to the thermal part, by adopting the one-point Gauss quadrature rule to proceed with the spatial integration, one can discretize Eq. (24) as:

$$\rho(\mathbf{x}_i)\ddot{\mathbf{u}}(\mathbf{x}_i,t)=\sum_{j=1}^{N}\mathbf{f}\left(\mathbf{u}(\mathbf{x}_j,t)-\mathbf{u}(\mathbf{x}_i,t),\mathbf{x}_j-\mathbf{x}_i\right)\beta(\mathbf{x}_j-\mathbf{x}_i)V_j+\mathbf{b}(\mathbf{x}_i,t) \tag{30}$$

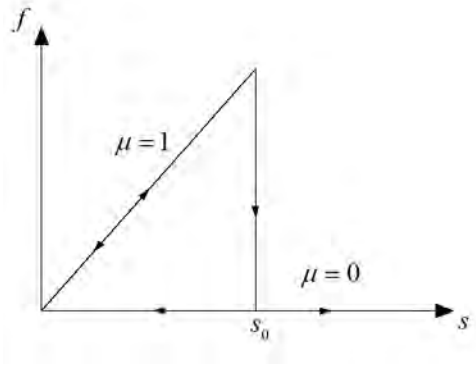

Figure 5: Linear-failure constitutive law for a PMB material.

where β is the volume correction factor which determines the portion of V_j that falls within the horizon of source node $\mathbf{x}_i$. In this paper, β value is determined as suggested in [54].

Remark 1. *Rather than using the volume correction factor β, it is possible to calibrate the influence function $\omega(\xi)$ in Eq. (25) to match the choice of m and the lattice configuration. In fact, one may use $m = 1$ on a hexagonal lattice to obtain exact integration for homogeneous deformation fields [55, 56]. This might be considered in future studies.*

In the present study, the quasi-static solution is achieved by means of the dynamic relaxation method introduced in [57]. As suggested in [58, 59], one may assemble the equation of motion of each node, Eq. (30), into a global system of equations and thus by introducing an artificial damping to the system, it can be concluded:

$$\mathbf{\Lambda}\ddot{\mathbf{U}}(\mathbf{X},t) + C\mathbf{\Lambda}\dot{\mathbf{U}}(\mathbf{X},t) = \mathbf{F}(\mathbf{U},\mathbf{U}',\mathbf{X},\mathbf{X}') \tag{31}$$

where $\mathbf{\Lambda}$ is the fictitious diagonal density matrix and C represents the damping coefficient; moreover, the positions vector, $\mathbf{X}$ and displacements vector $\mathbf{U}$ in Eq. (31) are expressed by:

$$\mathbf{X} = \langle \mathbf{x}_1, \mathbf{x}_2, \dots, \mathbf{x}_M \rangle \tag{32}$$

$$\mathbf{U} = \langle \mathbf{u}(\mathbf{x}_1,t), \mathbf{u}(\mathbf{x}_2,t), \dots, \mathbf{u}(\mathbf{x}_M,t) \rangle \tag{33}$$

in which, M is the total number of nodes and $\mathbf{F}$ represents the summation of the external and internal forces, which its i-th component is given by:

$$\mathbf{F}_i = \sum_{i=1}^{M} \sum_{j=1}^{N} \mathbf{f}\left(\mathbf{u}(\mathbf{x}_j, t) - \mathbf{u}(\mathbf{x}_i, t), \mathbf{x}_j - \mathbf{x}_i\right) \beta(\mathbf{x}_j - \mathbf{x}_i) V_j + \mathbf{b}(\mathbf{x}_i, t) \tag{34}$$

There are various ways to determine the density matrix, $\mathbf{\Lambda}$. In this study, it is taken as recommended in [59]. The values for damping ratio C is taken, $10^6 \sim 10^7 \mathrm{kg}/(\mathrm{m}^3\mathrm{s})$, as proposed by [58].

In the present study, time integration is performed by using the central difference explicit integration. Given displacement and acceleration of each node $\mathbf{x}_i$ at t^n, i.e. $\mathbf{u}_i^n$ and $\ddot{\mathbf{u}}_i^n$, velocities and displacements at $t^{n+1} = t^n + \Delta t_{ME}$ can be obtained by:

$$\dot{\mathbf{u}}_i^{n+1/2} = \frac{\left(2 - C\Delta t_{ME}\right) \dot{\mathbf{u}}_i{}^{n-1/2} + 2\Delta t_{ME} \mathbf{\Lambda}_i^{-1} \mathbf{F}_i^n}{2 + C\Delta t_{ME}} \tag{35}$$

$$\mathbf{u}_i^{n+1} = \mathbf{u}_i^n + \Delta t_{ME} \dot{\mathbf{u}}_i^{n+1/2} \tag{36}$$

$$\dot{\mathbf{u}}_i^{n+1} = \dot{\mathbf{u}}_i^{n+1/2} + \frac{\Delta t_{ME}}{2} \ddot{\mathbf{u}}_i^{n+1} \tag{37}$$

Hence, the solver can advance to the next time step by:

$$\mathbf{u}_i^{n+1} = \mathbf{u}_i^n + \Delta t_{ME} \dot{\mathbf{u}}^n{}_i + \frac{1}{2} \Delta t_{ME}^2 \ddot{\mathbf{u}}^n{}_i \tag{38}$$

where Δt_{ME} stands for the constant mechanical time step; likewise, to proceed in time the velocity at $t^{1/2}$ is given by:

$$\dot{\mathbf{u}}_i^{1/2} = \frac{1}{2} \Delta t_{ME} \mathbf{\Lambda}_i^{-1} \mathbf{F}_i^0 \tag{39}$$

As recommended in [59], for the mechanical part, the time step used for the dynamic relaxation method is set to 1, i.e. $\Delta t_{ME} = 1$; however, in thermo-mechanical coupling the time step, Δt, should be less than both mechanical and thermal time steps as:

$$\Delta t < \min\left\{\Delta t_{ME}, \Delta t_{TH}\right\} \tag{40}$$

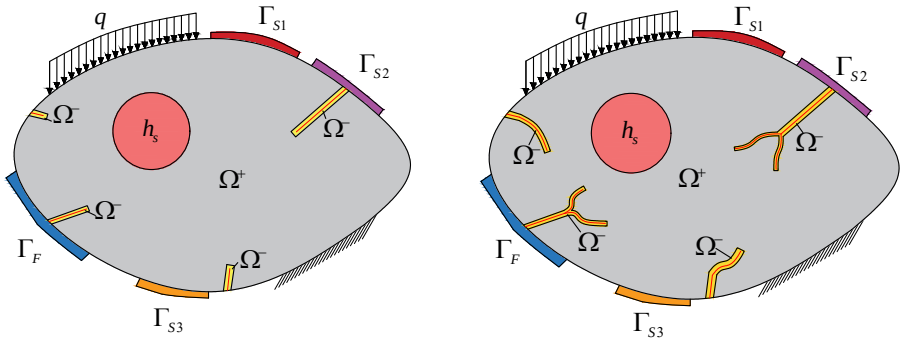

Figure 6: Adaptive refinement strategy.

3. Problem description

3.1. Coupling grids with different grid spacing

Using this technique, one is able to couple any two peridynamic grids with different grid spacing. This technique is applicable to both mechanical and thermal parts. To illustrate, a 1D problem domain, consisting of discretized parts with different grid spacing, is depicted in Figure 7. To this end, the solution domain, Ω, is divided into two sub-domains Ω^+ and Ω^-. Both sub-domains are simultaneously discretized by a coarse grid spacing Δx^+ characterized by a horizon δ^+ and a fine grid spacing $\Delta x^- < \Delta x^+$ characterized by a horizon δ^-. The nodes of the coarse grid in Ω^+ are the (initial) real nodes depicted by the green squares whereas those of the fine grid in Ω^- are the (initial) real nodes represented by the yellow circles (see Figure 7). The initial model is completed by the fictitious nodes. These fictitious nodes for the coarse and fine grid spacing zones are represented by unfilled-dashed squares and circles respectively as shown in Figure 7. Moreover, the red squares and circles shown in Figure 7, stand for the activated fictitious nodes where the two sets of grids are coupled. In fact, the activated fictitious nodes are used to make the real nodes located near the interface between the parts, seem surrounded by a complete horizon (of their own type). The curved lines demonstrate the peridynamic bond interactions. In Figure 7, m ratio is 2, i.e. each node interacts with two nodes on each side. Although various m values and horizon sizes

can be adopted in this model, for the sake of simplicity the horizon size is taken equal to $\delta = 2\Delta x$. Fictitious nodes are activated on the boundaries of the two sub-domains where the two grid spacing are supposed to be coupled. The distance, l_0, between the two portions is considered to be smaller than both δ^+ and δ^-. In this study, it is assumed that the sub-domain Ω^- grows only where it is essential (see Figure 6). In this way, the algorithm is used in order to efficiently optimize the use of computational resources. Hence, by using this method, the problem of surface effect in the interface zone between parts with different grid spacing is solved.

The stiffness matrix of a bond between two generic nodes, $\mathbf{x}_i$ and $\mathbf{x}_j$, based on the small deformation assumption, is given by:

$$\mathbf{k} = \frac{c_{ME,\,TH}}{|x_j - x_i|}\beta(x_j - x_i)V_iV_j\begin{bmatrix} 1 & -1 \\ -1 & 1 \end{bmatrix} \tag{41}$$

As for instance, node 3 (in Figure 7) represents a node interacting only with the real nodes; the corresponding equations of equilibrium can be written by:

$$\begin{cases} -\alpha_{31}k^+_{ME}u_1 - \alpha_{32}k^+_{ME}u_2 + \left(\alpha_{31}+\alpha_{32}+\alpha_{34}+\alpha_{35}\right)k^+_{ME}u_3 - \alpha_{34}k^+_{ME}u_4 - \alpha_{35}k^+_{ME}u_5 = F_3 \\ -\alpha_{31}k^+_{TH}\theta_1 - \alpha_{32}k^+_{TH}\theta_2 + \left(\alpha_{31}+\alpha_{32}+\alpha_{34}+\alpha_{35}\right)k^+_{TH}\theta_3 - \alpha_{34}k^+_{TH}\theta_4 - \alpha_{35}k^+_{TH}\theta_5 = h_{s(3)} \end{cases} \tag{42}$$

in which:

$$\alpha_{ij} = \frac{\beta(x_j - x_i)}{|x_j - x_i|} \tag{43}$$

F_i and $h_{s(i)}$ are the external force and heat source applied to node $\mathbf{x}_i$; in addition, $k^+_{ME} = c^+_{ME}V_i^+V_j^+$ and $k^+_{TH} = c^+_{TH}V_i^+V_j^+$. However, for the nodes connected to active fictitious nodes, some non-standard terms appear in the equilibrium equations. For instance, the equilibrium equations of node 4 are:

$$\begin{cases} -\alpha_{42}k^+_{ME}u_2 - \alpha_{43}k^+_{ME}u_3 + \left(\alpha_{42}+\alpha_{43}+\alpha_{45}+\alpha_{46}\right)k^+_{ME}u_4 - \alpha_{45}k^+_{ME}u_5 - \alpha_{46}k^+_{ME}u_6 = F_4 \\ -\alpha_{42}k^+_{TH}\theta_2 - \alpha_{43}k^+_{TH}\theta_3 + \left(\alpha_{42}+\alpha_{43}+\alpha_{45}+\alpha_{46}\right)k^+_{TH}\theta_4 - \alpha_{45}k^+_{TH}\theta_5 - \alpha_{46}k^+_{TH}\theta_6 = h_{s(4)} \end{cases} \tag{44}$$

The displacement and temperature at node 6 (u_6, θ_6), can be obtained by a linear interpolation between nodes e and f. Therefore, Eq. (44) takes the following form:

$$\begin{cases} -\alpha_{42}k^+_{ME}u_2 - \alpha_{43}k^+_{ME}u_3 + \left(\alpha_{42}+\alpha_{43}+\alpha_{45}+\alpha_{46}\right)k^+_{ME}u_4 - \alpha_{45}k^+_{ME}u_5 - \alpha_{46}k^+_{ME}\left(c_eu_e + c_fu_f\right) = F_4 \\ -\alpha_{42}k^+_{TH}\theta_2 - \alpha_{43}k^+_{TH}\theta_3 + \left(\alpha_{42}+\alpha_{43}+\alpha_{45}+\alpha_{46}\right)k^+_{TH}\theta_4 - \alpha_{45}k^+_{TH}\theta_5 - \alpha_{46}k^+_{TH}\left(c_e\theta_e + c_f\theta_f\right) = h_{s(4)} \end{cases} \tag{45}$$

in which, c_e and c_f are the linear combination coefficients related to the values of the geometric parameters of the two grids. Similarly, the equilibrium equations for node 5 take the following form:

$$\begin{cases} -\alpha_{53}k^{+}_{ME}u_3 - \alpha_{54}k^{+}_{ME}u_4 + \left(\alpha_{53}+\alpha_{54}+\alpha_{56}+\alpha_{57}\right)k^{+}_{ME}u_5 - \alpha_{56}k^{+}_{ME}\left(c_e u_e + c_f u_f\right) - \alpha_{57}k^{+}_{ME}\left(c_g u_g + c_h u_h\right) = F_5 \\ -\alpha_{53}k^{+}_{TH}\theta_3 - \alpha_{54}k^{+}_{TH}\theta_4 + \left(\alpha_{53}+\alpha_{54}+\alpha_{56}+\alpha_{57}\right)k^{+}_{TH}\theta_5 - \alpha_{56}k^{+}_{TH}\left(c_e\theta_e + c_f\theta_f\right) - \alpha_{57}k^{+}_{TH}\left(c_g\theta_g + c_h\theta_h\right) = h_{s(5)} \end{cases} \tag{46}$$

In an analogous way, for a node located in the fine grid zone and connected to the activated fictitious nodes, for example node e, the equilibrium equations are given by:

$$\begin{cases} -\alpha_{ec}k^{-}_{ME}u_c - \alpha_{ed}k^{-}_{ME}u_d + \left(\alpha_{ec}+\alpha_{ed}+\alpha_{ef}+\alpha_{eg}\right)k^{-}_{ME}u_e - \alpha_{ef}k^{-}_{ME}u_f - \alpha_{eg}k^{-}_{ME}u_g = F_e \\ -\alpha_{ec}k^{-}_{TH}\theta_c - \alpha_{ed}k^{-}_{TH}\theta_d + \left(\alpha_{ec}+\alpha_{ed}+\alpha_{ef}+\alpha_{eg}\right)k^{-}_{TH}\theta_e - \alpha_{ef}k^{-}_{TH}\theta_f - \alpha_{eg}k^{-}_{TH}\theta_g = h_{s(e)} \end{cases} \tag{47}$$

and it becomes:

$$\begin{cases} -\alpha_{ec}k^{-}_{ME}\left(c_4u_4 + c_5u_5\right) - \alpha_{ed}k^{-}_{ME}\left(c_5u_5 + c_eu_e\right) + \left(\alpha_{ec}+\alpha_{ed}+\alpha_{ef}+\alpha_{eg}\right)k^{-}_{ME}u_e - \alpha_{ef}k^{-}_{ME}u_f - \alpha_{eg}k^{-}_{ME}u_g = F_e \\ -\alpha_{ec}k^{-}_{TH}\left(c_4\theta_4 + c_5\theta_5\right) - \alpha_{ed}k^{-}_{TH}\left(c_5\theta_5 + c_e\theta_e\right) + \left(\alpha_{ec}+\alpha_{ed}+\alpha_{ef}+\alpha_{eg}\right)k^{-}_{TH}\theta_e - \alpha_{ef}k^{-}_{TH}\theta_f - \alpha_{eg}k^{-}_{TH}\theta_g = h_{s(e)} \end{cases} \tag{48}$$

where $k^{-}_{ME} = c^{-}_{ME}V^{-}_{i}V^{-}_{j}$ and $k^{-}_{TH} = c^{-}_{TH}V^{-}_{i}V^{-}_{j}$.

To conserve the total mass of the system, it is essential to calculate the distance between the parts of the model, l_0, as follows [49]:

$$l_0 = \frac{\Delta x^{+} + \Delta x^{-}}{2} \tag{49}$$

For 2D and 3D cases, the same approach is applicable. As shown in Figure 8, the square domain is discretized by two different grid spacing. In Figure 8, the fine and coarse grids are disconnected and we use $m = 2$; although different values of m can be considered. The grid spacing in the coarse and fine grids are represented by Δx^{-} and Δx^{+}, respectively. Accordingly, the horizon sizes of the two parts are: $\delta^{+} = 2\Delta x$ and $\delta^{-} = 2\Delta x^{-}$. In Figure 8, node A represents a real node of the fine grid which locates near the coupling zone. This node should interact with all the real and the fictitious nods of its own type (nods of the fine grid) located in its horizon, δ^{-}. The red circle nodes are the activated fictitious nodes whose values should be determined by the linear interpolation of the four real nearest family nodes surrounding them. Furthermore, node

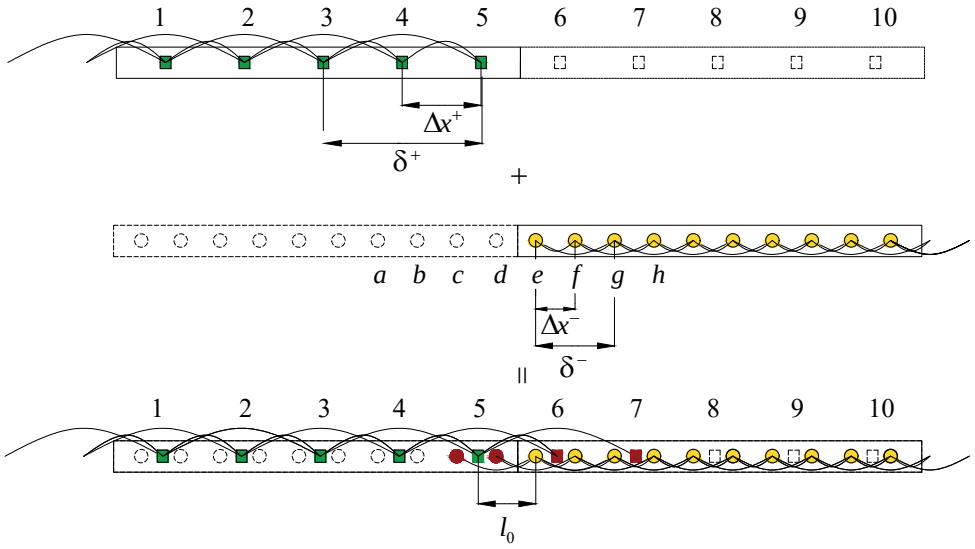

Figure 7: The coupling strategy in 1D problem.

B represents a real node of the coarse grid which locates near the coupling zone as shown in Figure 8. It also interacts with the family nodes of its own type located in its horizon. Red square nodes are the activated fictitious nodes whose displacements are interpolated by the bi-linear interpolation of the four real nearest family nodes. After finding the displacement of the fictitious activated nodes, one is able to calculate the forces acting on the real nodes. It should be pointed out that the present scheme can readily be extended to 3D problems.

3.2. Adaptive refinement

By means of the aforementioned coupling method, one may apply a fine grid in the zones where cracks are prone to nucleate or propagate, while in the remaining parts of the body a coarse grid is used. Moreover, it is very efficient to expand the fine grid adaptively where large strain gradients are present. To achieve this, a switching algorithm is required. The reader is referred to [49] for the details. The algorithm is triggered when a bond stretch in coarse grid exceeds a critical value. It is designed such that the crack tip never reaches the zones discretized by the coarse grid. Considering

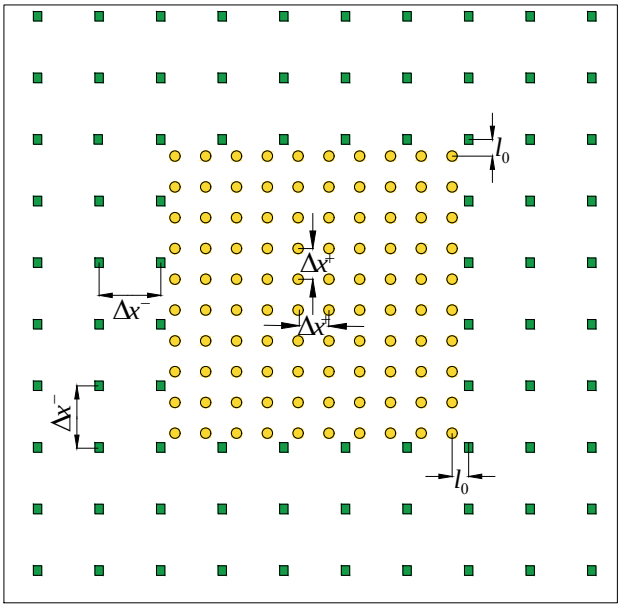

(a)

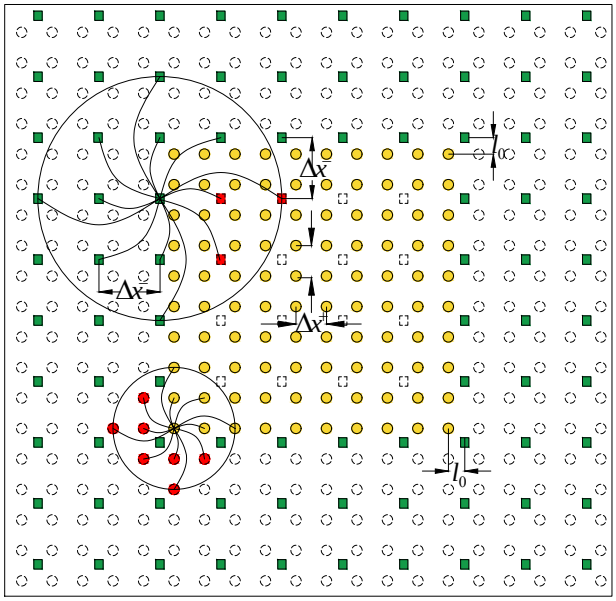

(b)

Figure 8: (a) Two still disconnected portions of a 2D model discretized by two different grid spacing, and (b) introduction of fictitious nodes to connect the portions.

two generic nodes in the coarse grid zone as $\mathbf{x}_i$ and $\mathbf{x}_j$, one may write the stretch of the bond linking them at the time, t_n, as follows (see Figure 9a):

$$s_{ij}^n = \frac{\left\| (\mathbf{x}_j + \mathbf{u}_j^n) - (\mathbf{x}_i + \mathbf{u}_i^n) \right\|}{\left\| \mathbf{x}_j - \mathbf{x}_i \right\|} - 1 \tag{50}$$

Nodes $\mathbf{x}_i$ and $\mathbf{x}_j$ are referred to as *critical nodes* when s_{ij}^n satisfies the following relation:

$$\chi s_0 \leqslant s_{ij}^n - \alpha T_{avg} \leqslant s_0, \quad 0 < \chi < 1 \tag{51}$$

in which χ is the switching factor. The higher values of χ, the narrower zone of a coarse grid is modified by the fine grid. In contrast, a larger zone of the coarse grid should be transformed to a fine grid by using the smaller values of χ. The domain discretization after application of the switching algorithm is depicted in Figure 9b. Since displacements, velocity and acceleration have to be assigned to the previously inactive nodes, the values are interpolated from the surrounding nodes.

4. The step-by-step procedure of the method

1. Define the constant parameters:
   - Mechanical constants: E, ν, ρ, Δt_{ME}, δ, c_{ME}, C.
   - Thermal constants: c_v, γ, α, θ_0, θ_∞, Δt_{TH}, δ, c_{TH}.
   - As recommended in [59], for the mechanical part set Δt_{ME} equal to 1. Furthermore, in thermo-mechanical coupling Δt should be less than both mechanical and thermal time increments, $\Delta t < \min\left\{\Delta t_{ME}, \Delta t_{TH}\right\}$
2. Pre-processing:
   - Build the grid sets, define node type, horizon sets, mark the fictitious nodes, define pre-cracks.
   - Applying the mechanical and the thermal initial conditions.
3. Thermal analysis for step $(n+1)$ and evaluate, θ^{n+1}, by Eq. (8).
4. Evaluate the displacements of the real nodes using the dynamic relaxation scheme through Eqs. (31)-(38).

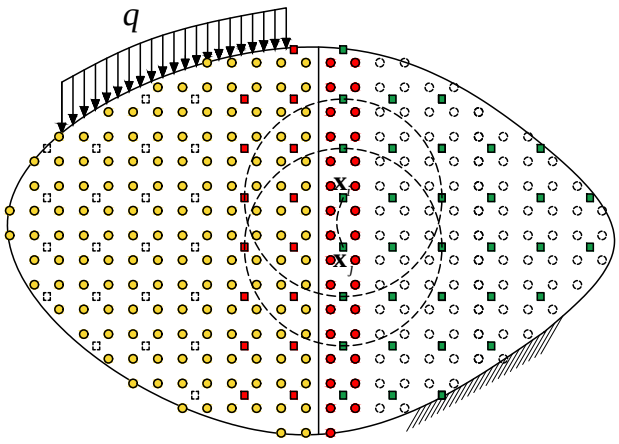

(a)

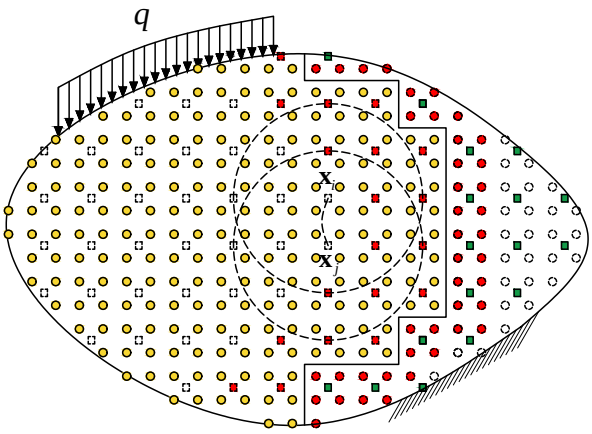

(b)

Figure 9: Variation of the model within two consecutive time steps; (a) the curved bond is the one that identifies two critical nodes of the coarse grid, (b) the coupled model after the refinement.

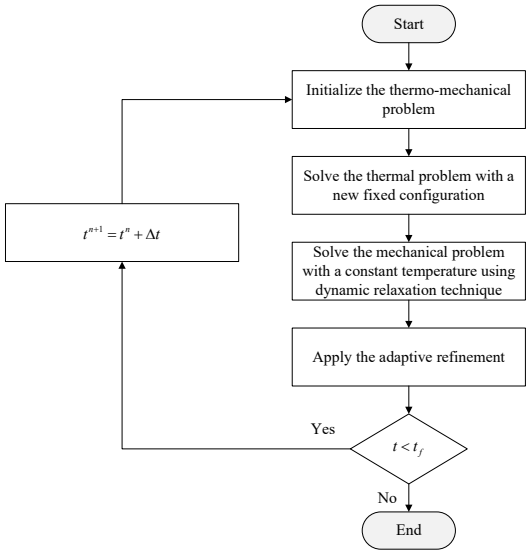

Figure 10: Step by step procedure of the method.

5. Calculate displacement of the fictitious nodes, $\mathbf{u}_i^{n+1}$, using linear or bi-linear interpolation.
6. Calculate the stretch of the active bonds in the fine grid zone by Eq. (23).
7. Check if the stretch of the bonds exceeds its critical value, based on Eq. (28), the bond should be broken and removed from the calculations.
8. Evaluate the damage level of the real nodes in the fine grid zone using Eq. (29).
9. Calculate the stretch of the active bonds in the coarse grid zone by Eq. (50).
10. Check if the stretch of the bonds in coarse grid is within the range defined in Eq. (51), mark the node to be switched from coarse to fine.
11. Apply the refinement technique as described in section 3.2.
12. Save the updated displacements and temperature values as the initial values for the next time step.
13. Repeat from step 3 for the next time step.

The whole solution procedure is visualized in the flowchart shown in Figure 10.

5. Numerical Examples

To examine the performance of the present approach, a set of numerical examples are solved. To this end, an in-house C++ code is developed. The timings reported (which excluds I/O times) are measured on an Intel Core i7-6700HQ 2.60 GHz CPU, running 64 bit Windows 10 Enterprise. To compile the code, Microsoft Visual C++ 2015 compiler is used, which lets us leverage the power of multi-core CPU using OpenMP directives.

5.1. Example I: Thermo-mechanical analysis of a plate with a hole

In this example, deformation of a plate with a hole, due to non-uniform heating, is investigated; no crack propagation is considered (see Figure 11). We determine the temperature distribution over the domain and boundaries. Correspondingly, deformation is evaluated by using the dynamic relaxation method. This benchmark has been investigated in [60]. A plate with the dimensions of $L \times W$ is considered here. The problem is solved in a plane stress condition with $L = 0.15$ m, $W = 0.05$ m, $E = 200 \times 10^9$ Pa, $\alpha = 16 \times 10^{-6}\,\mathrm{K}^{-1}$, $\rho = 7850\,\mathrm{kg/m}^3$ and $\nu = 1/3$. The plate has a thermal conductivity $\gamma = 20\,\mathrm{W/mK}$, and specific heat $c_v = 500\,\mathrm{J/kgK}$. The initial temperature of the plate is 20 °C. The right and left boundaries are subjected to constant temperatures as: $\theta^*(x = -L/2, y, t) = 500\,°\mathrm{C}$ and $\theta^*(x = L/2, y, t) = 20\,°\mathrm{C}$. The remaining boundaries are insulated. Moreover, $m = 3$ is used to solve this example.

To impose the mechanical boundary conditions, the left and the right sides of the plate are subjected to zero displacement constraints as: $u(x = -L/2, y, t) = 0$, $u(x = L/2, y, t) = 0$, whereas other boundaries are free of tractions. This example is solved for a duration of $t = 1000\,\mathrm{s}$ with the time integration interval of $\Delta t = 0.01\,\mathrm{s}$, which results in 100000 steps.

The plate is discretized in three different ways: Uniform, Non-uniform I and Non-uniform II. In the Uniform model the grid spacing is $\Delta x = \Delta y = 5 \times 10^{-4}$ m. Non-uniform I is a coupled model with $\Delta x^+ = 10^{-3}$ m and $\Delta x^- = 5 \times 10^{-4}$ m. Additionally, Non-uniform II is a coupled model with $\Delta x^+ = 10^{-3}$ m and $\Delta x^- = 0.25 \times 10^{-4}$ m. The fine parts are shown in Figure 11 by Ω^-. The fine parts are chosen randomly without any

symmetry axis. The fine grid zones in Figure 11 are neither parallel nor perpendicular to the plate sides. To obtain the converged solution, initially this model is simulated with the Uniform grid model. Finding the proper value of Δx, we compare the contour plots of the temperature and horizontal displacement in Figures 12-13. The results of the Non-uniform I and Non-uniform II model are in an excellent agreement with the Uniform one. Moreover, the plate is simulated in Abaqus 6.13 by the finite element method (FEM). Then, the temperature profile and displacements contour plots are compared with the BB-PD results. The comparison indicates a remarkable agreement. We define a relative displacement and temperature error as:

$$e_u = \frac{\left|u - u_{ref}\right|}{\left|u_{ref}\right|} \times 100 \tag{52}$$

and

$$e_\theta = \frac{\left|\theta - \theta_{ref}\right|}{\left|\theta_{ref}\right|} \times 100 \tag{53}$$

in which, θ_{ref} and u_{ref} stand for the temperature and displacement (along x or y axis) of the reference solution (FEM). Then, the relative temperature and displacement (along x direction) error contour plots for the Non-uniform II are depicted in Figure 14. The maximum relative error for the displacement along x direction, e_u, and the maximum relative error of the temperature, e_θ, are not more than 4.5% and 2% respectively (see Figure 14). This inevitable error, which is due to the surface effects of the peridynamic approach, occurs near the boundaries of the domain.

For further validation of the present method, two nodes, $\mathbf{x}_A = (0.035, 0.005)$ and $\mathbf{x}_B = (0.04, 0.0085)$ are chosen to investigate the time history of the horizontal displacement and temperature in all three models. The time history of the horizontal displacement for nodes $\mathbf{x}_B$ and $\mathbf{x}_A$ are shown in Figure 15a and Figure 15b, respectively. The results for both of the nodes are in an acceptable agreement; however, better agreement of the three models can be observed for node B. Moreover, the time history of the temperature for nodes $\mathbf{x}_B$ and $\mathbf{x}_A$ are depicted in Figure 15c and Figure 15d, respectively. The results are in an excellent agreement and no significant numerical perturbation can be observed.

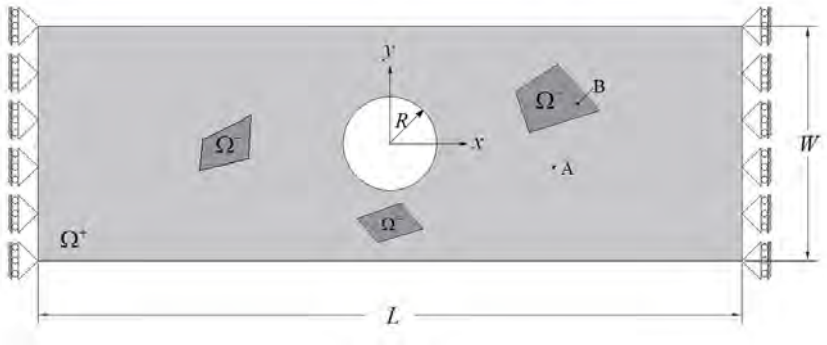

Figure 11: Problem domain, boundary conditions, and the zones with fine grid in Example I.

5.2. *Example II: Pre-cracked disk specimen under central thermal shock*

In this example, we investigate the thermo-mechanical crack propagation in a pre-cracked disk using the adaptive multi-grid peridynamic method. This example has already been used as an experimental test to measure the thermal-shock resistance of different materials such as ceramics [4, 5, 61]. In this test, the center of a disk is heated at its both sides over a circular area as depicted in Figure 16. Due to the central constant heat flux and the existence of the pre-crack, the inhomogeneous temperature distribution occurs over the disk which leads to the inhomogeneous thermal expansion and stress in the domain. The thermal shock fracture takes place when the emerged tensile stress reaches a certain value.

Based on the experiments conducted in [4, 5, 61], three different crack paths are observed in Figure 17. The first type of the crack path is a straight line from the pre-crack to the opposite side of the disk as depicted in Figure 17(a). The second type of the crack path begins from the pre-notched crack tip propagates into two branches inside the heating area as shown in Figure 17(b). The third type of the crack path resembles the second one; however, the crack branches outside of the heating area as depicted in Figure 17(c). This example also has been solved using phase filed numerical solution in [19] and all three types of crack paths have been observed.

As shown in Figure 16, the radius of the disk and the pre-notched crack size are chosen as: $R = 0.015\,\mathrm{m}$ and $a = 0.002\,\mathrm{m}$. Regarding the data available in literature

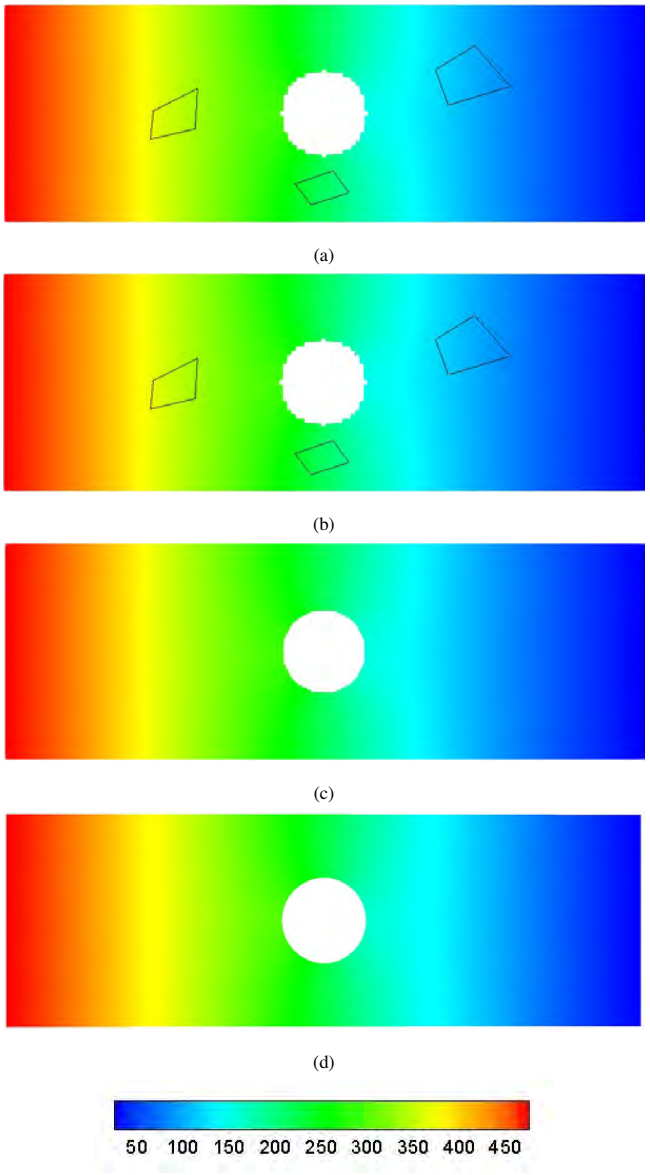

Figure 12: Temperature ($T[^{\circ}C]$) after 1000 s: (a) Non-uniform I PD (b) Non-uniform II PD (c) Uniform PD and (d) FEM models.

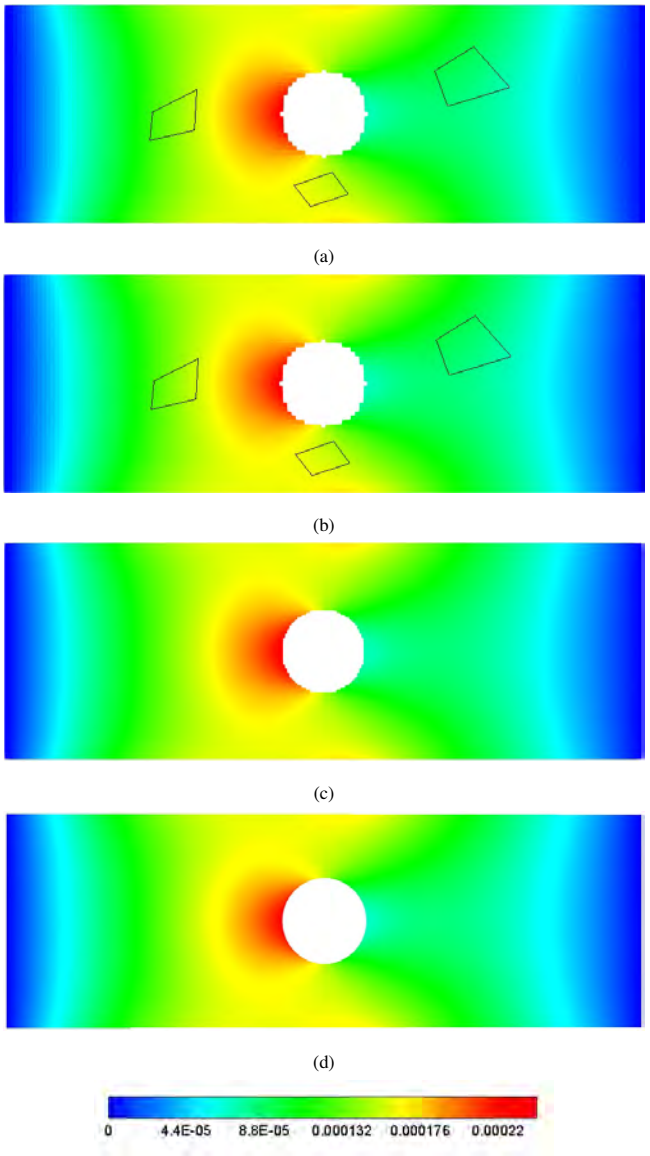

Figure 13: Displacement (u_x [m]) after 1000 s: (a) Non-uniform I PD (b) Non-uniform II PD(c) Uniform PD and (d) FEM models.

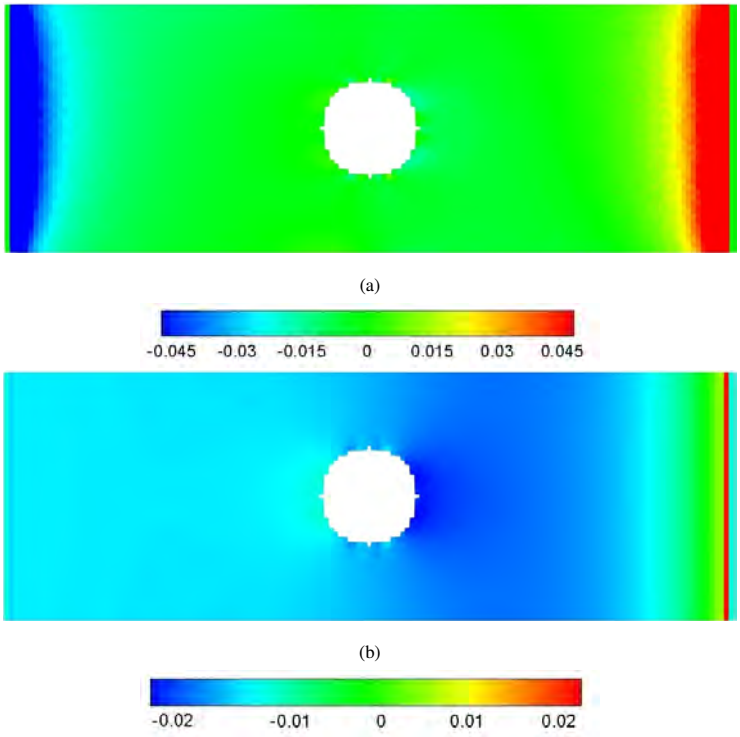

Figure 14: (a) Relative displacement error (e_u) in x direction (b) relative temperature error (e_θ) for Non-uniform II PD.

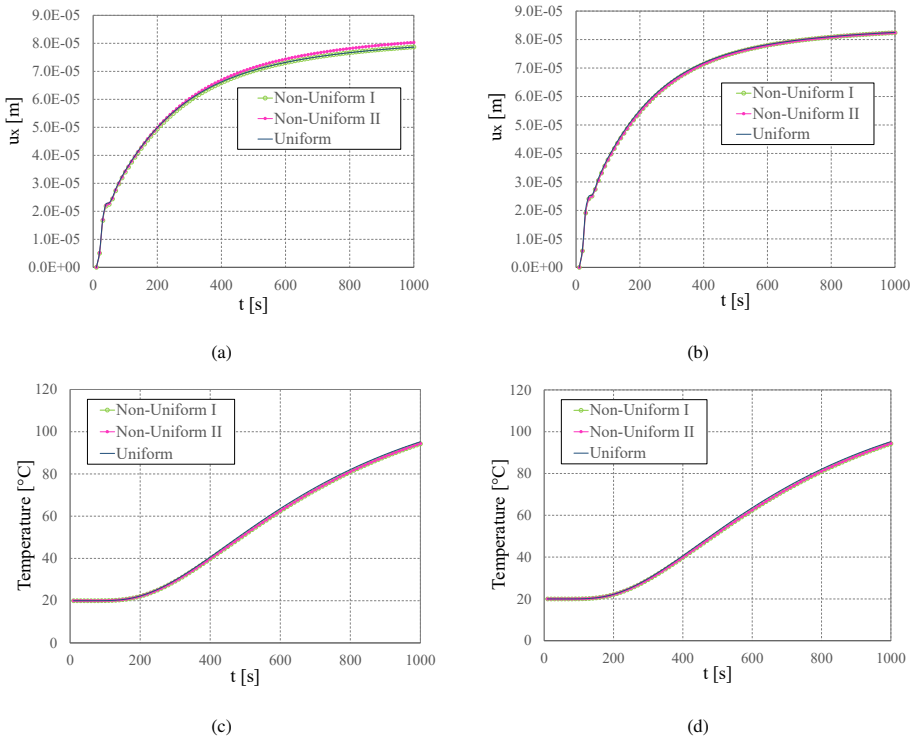

Figure 15: The time history of (a) horizontal displacement of node $\mathbf{x}_B$ (b) horizontal displacement of node $\mathbf{x}_A$ (c) temperature of node $\mathbf{x}_B$ (d) temperature of node $\mathbf{x}_A$

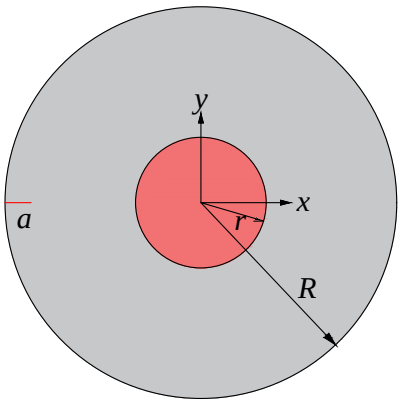

Figure 16: Geometry and boundary conditions for the thermal shock fracture problem in a disk. The red area denotes an imposed body heat flux.

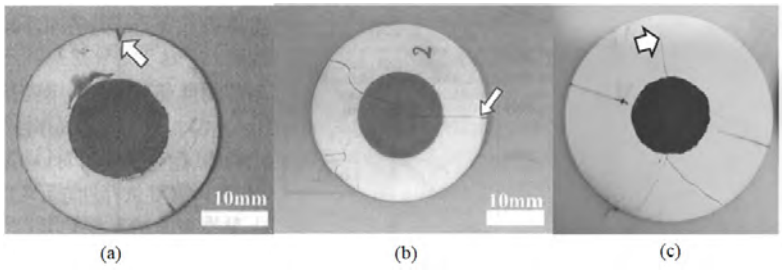

Figure 17: Three types of crack paths in experiments from [4, 5]; (a) crack grows straightly through the heating area (b) crack branches in the heating area (c) crack branches outside of the heating area.

[5], the problem is solved in a plane stress condition with $E = 380 \times 10^9\,\mathrm{Pa}$, $\alpha = 6.6 \times 10^{-6}\,\mathrm{K}^{-1}$, $\rho = 3900\,\mathrm{kg/m^3}$, $G_c = 26.95\,\mathrm{J/m^2}$ and $\nu = 1/3$. The plate has a thermal conductivity $\gamma = 21\,\mathrm{W/mK}$, and specific heat $c_v = 961.5\,\mathrm{J/kgK}$. An adiabatic boundary condition is imposed around the disk. The value of the central heat flux in Eq. (8) is $h_s = \gamma\,\mathrm{kW/m^3}$, the radius of the heating area is r as depicted in Figure 16. Furthermore, $m = 3$ is used to solve this example.

A uniform peridynamic model with a grid spacing of $\Delta x = 0.0003\,\mathrm{m}$ is taken as the reference solution. The adaptive refinement solution is considered by using a refined model ($\Delta x^- = 0.0003\,\mathrm{m}$ and $\Delta x^+ = 0.0006\,\mathrm{m}$). This example is solved for a duration of $t = 0.059\,\mathrm{s}$ with a time step of $\Delta t = 10^{-5}\,\mathrm{s}$, which results in 59000 steps. The radius of the heating part and the heat flux for this example are taken as: $\gamma = 750000\,\mathrm{kW/m^3}$ and $r = 5\,\mathrm{mm}$.

The contour plots of damage obtained by the proposed method and the uniform model at 6 different instants are depicted in Figure 18. Also, the temperature distribution of the uniform and the adaptive model is shown in Figure 19. A very good agreement in both cases is achieved. In Table 1, the runtime of each simulation with the number of real nodes reported.

To compare the proposed method with the phase field model introduced in [19], we perform a new simulation with a set of parameters shown in Figures 21d-21f. In all three cases, the obtained crack path by the present solution conforms to that of the phase field solution and the experimental results in Figure 17.

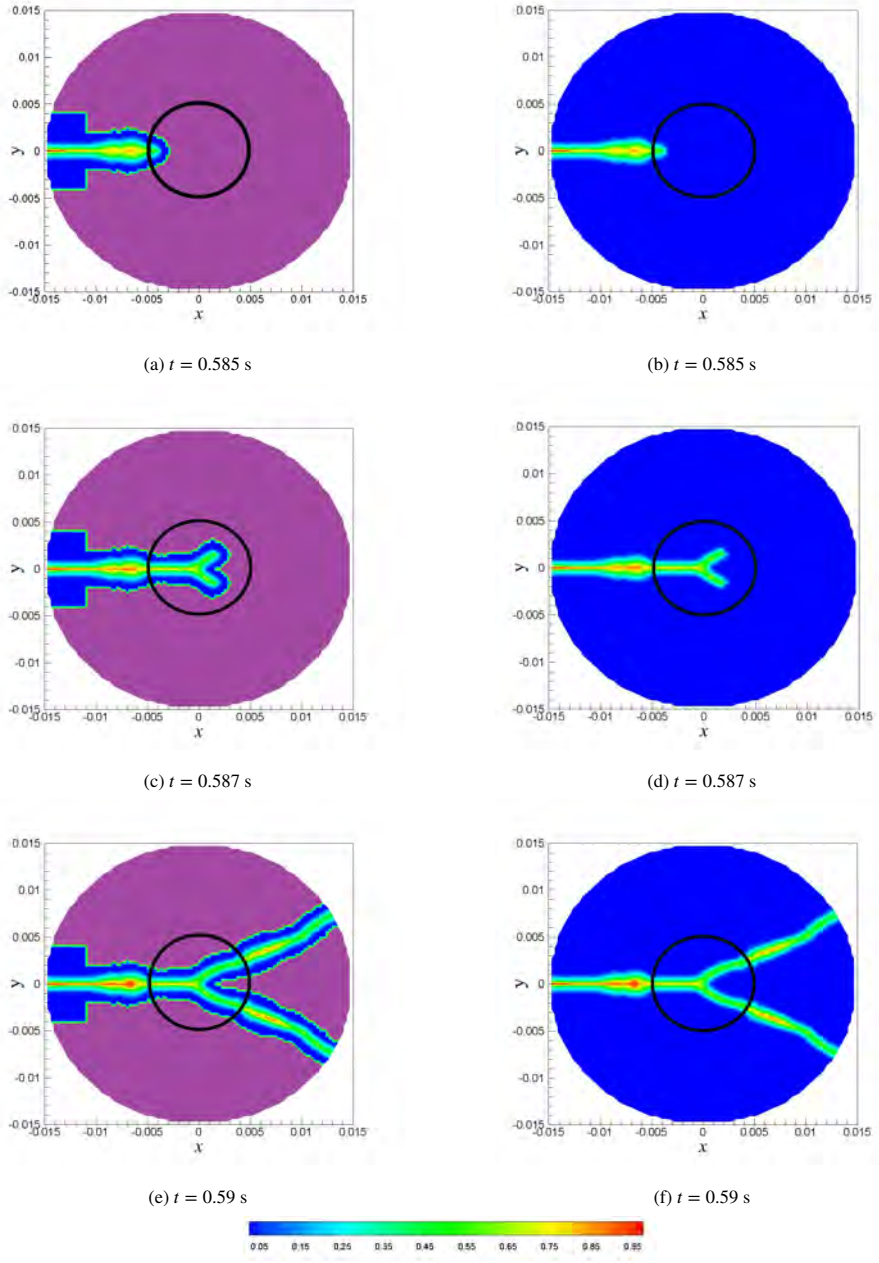

(a) $t = 0.585$ s (b) $t = 0.585$ s

(c) $t = 0.587$ s (d) $t = 0.587$ s

(e) $t = 0.59$ s (f) $t = 0.59$ s

Figure 18: Example II. Damage (ϕ) at different time instances (a), (c) and (e) in the adaptive model (b), (d) and (f) in the uniform model (damage only related to the fine grid).

Table 1: Comparison of the computational resources used by uniform and adaptive models in Example II.

	Number of real nodes		
		Adaptive	
	Uniform	Coarse	Fine
$t = 0$ s	7825	3741	343
$t = 0.59$ s		1833	2996
Run time	521.60 s	175.31 s	

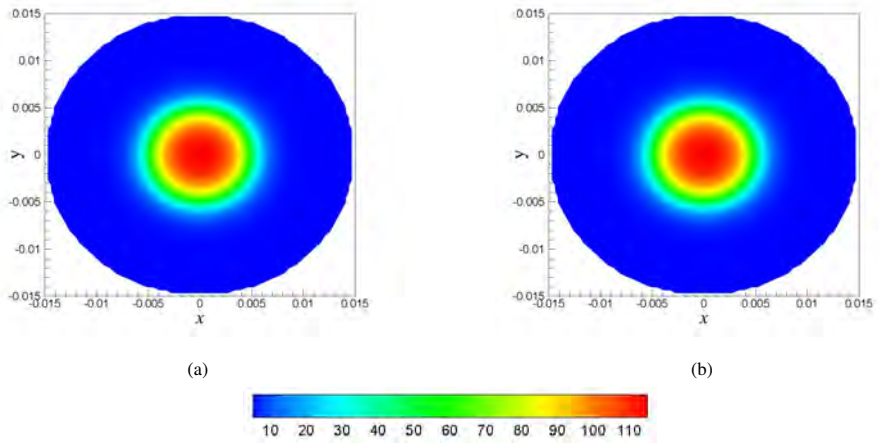

Figure 19: Example II: Temperature $T[^{\circ}C]$ after 0.59 s: (a) the adaptive model (b) the uniform model.

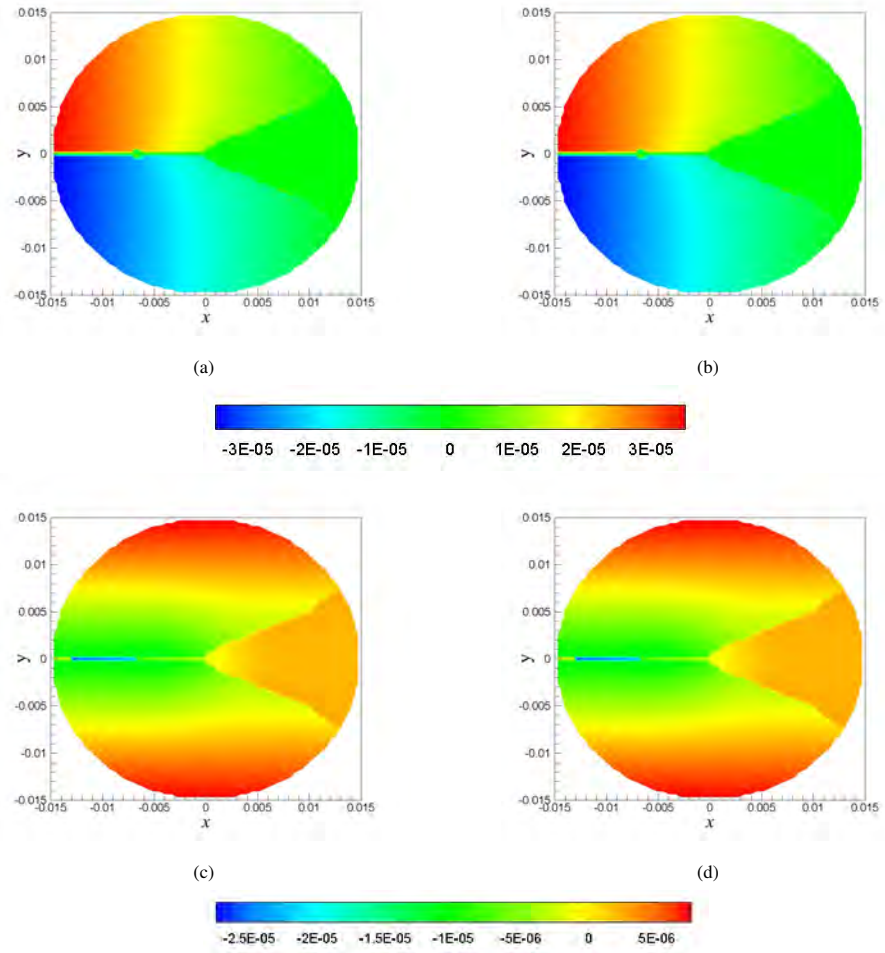

Figure 20: Example II: the vertical displacement (u_y [m]) after 0.59 s in (a) the adaptive model (b) the uniform model and the horizontal displacement (u_x [m]) after 0.59 s in (c) the adaptive model (d) the uniform model.

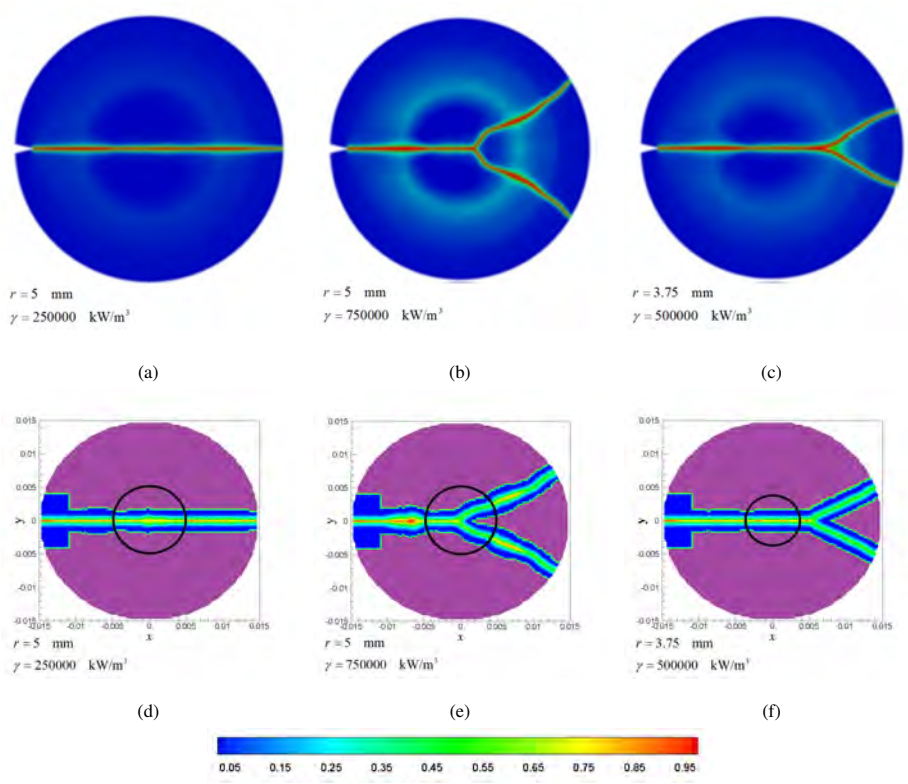

Figure 21: (a)-(c) Crack path (ϕ) in the phase field model [19] (d)-(e) the adaptive peridynamic model when the disk is broken completely.

5.3. Example III: Quenching test of rectangular specimen under central thermal shock

In this example, complex crack patterns induced by thermal shocks using the adaptive peridynamic model is investigated. The quenching test is a benchmark to measure the thermal shock resistance of different kinds of materials. In the experiments done by [3], rectangular ceramic slabs are heated to a certain temperature and then dropped into a water bath. Accordingly, some parallel cracks start to grow from the lateral surface of the slab due to the quenching phenomenon. The slabs with a higher initial temperature show extreme shrinkage and hence, more cracks with longer depth emerge on the boundaries of the slabs. For the first time, a method based on energy minimization has been established to calculate the periodic array and selective crack growth by [62]. Furthermore, other numerical simulation of this experiment can be traced in the literature (see for example [18, 19, 38, 40, 63, 64]); however, due to the complexity of the crack patterns, a large number of elements or nodes is needed which increases the computational cost drastically. Hence, we consider two models for this example; one uniform model with a fine grid spacing ($\Delta x = 0.00014\,\mathrm{m}$), and an adaptive model ($\Delta x^- = 0.00014\,\mathrm{m}$ and $\Delta x^+ = 0.00028\,\mathrm{m}$). Then, the accuracy of the adaptive model is investigated by comparing these two models with the experiment data.

The rectangular slab has the length of $L = 0.05\,\mathrm{m}$ and width of $W = 0.01\,\mathrm{m}$ as shown in Figure 22. Based on the experimental model in [3], the problem is solved in a plane strain condition with $E = 340 \times 10^9\,\mathrm{Pa}$, $\alpha = 7.2 \times 10^{-6}\,\mathrm{K}^{-1}$, $\rho = 3950\,\mathrm{kg/m}^3$, $G_c = 42.27\,\mathrm{J/m}^2$ and $\nu = 1/4$. The plate has a thermal conductivity $\gamma = 18\,\mathrm{W/mK}$, and specific heat $c_v = 880\,\mathrm{J/kgK}$. The convection boundary condition is imposed to the sides of the plate as depicted in Figure 22. This example is solved for a duration of $t = 1\,\mathrm{s}$ with a time step of $\Delta t = 10^{-5}\,\mathrm{s}$, which results in 100000 steps. Furthermore, $m = 3$ is used to solve this example. The initial temperature is taken as $\theta_0 = 680\,\mathrm{K}$, while the temperature of the surfaces contacted with water is $\theta_\infty = 300\,\mathrm{K}$.

The contour plots of the damage obtained by the adaptive model and the uniform model at $t = 1\,\mathrm{s}$ are represented in Figure 23. Qualitatively, an acceptable agreement is obtained between the crack paths of the models. Moreover, the experimental results of [3], depicted in Figure 23, are in a very good agreement with both peridynamic models.

In order to compare the crack paths quantitatively, one may analyze the crack fre-

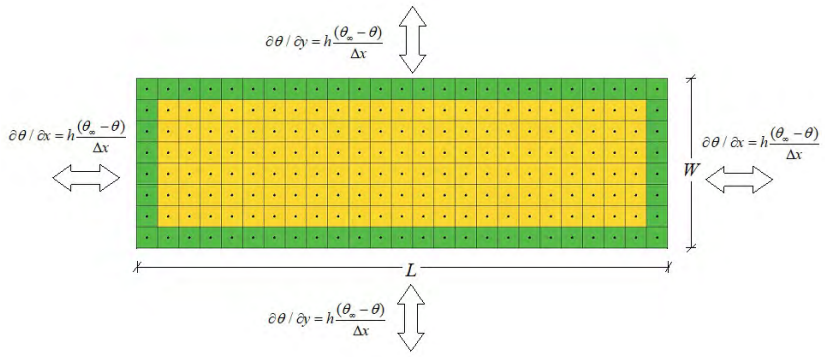

Figure 22: Example III: Numerical model of the ceramic specimen subjected to 2D heat transfer.

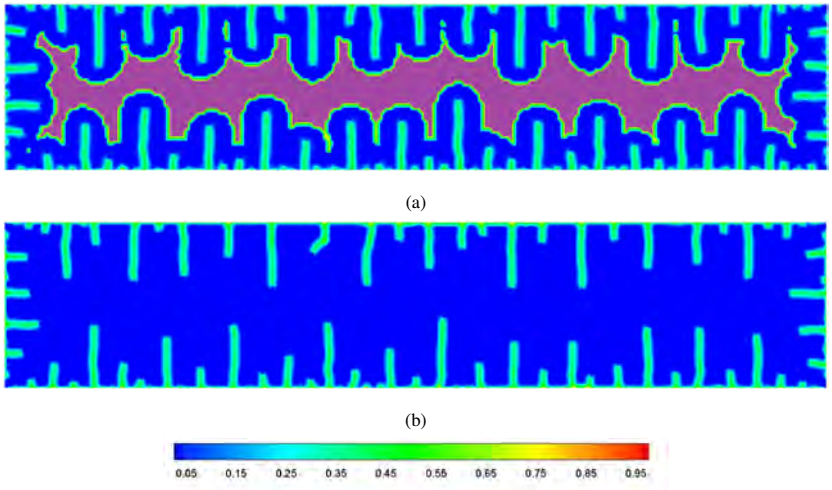

Figure 23: Example III: Damage (ϕ) after 1.00 s: (a) the adaptive model (b) the uniform model (damage only related to the fine grid).

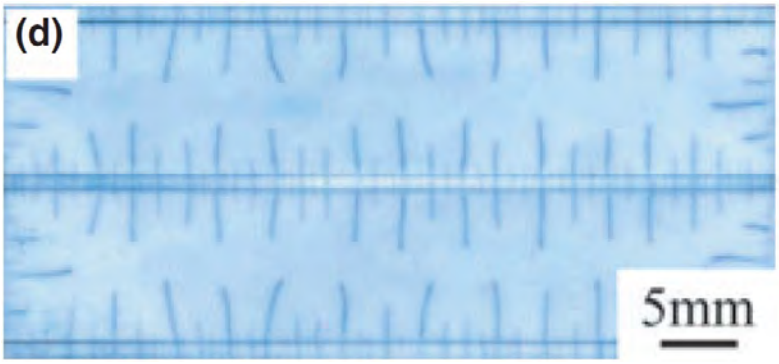

Figure 24: Experimental results of quenching test by [3].

quency chart as shown in Figure 25. For this analysis only the cracks whose length is greater than 10% of the plate half-width are considered. In the study by [38], this example has been solved by an OSB-PD model and the results have been compared to the experimental results. In the results reported in [38], the number of total cracks with the length of $0.05-0.45$ mm is 52 while it is 56 in the experiment. In this study, 55 and 57 cracks have been obtained using the adaptive model and the uniform model, respectively. The obtained results reveal that the present method performs well and exhibits solutions in a good agreement with those obtained in the experiment. Analyzing Figure 25, one can conclude that the crack frequency trend line (dotted line) in the adaptive refined model is much more in agreement with the experimental data compared with other referred models.

Additionally, in Table 2, the runtime of each simulation and the number of real nodes are reported. Consequently, the proposed adaptive technique not only reduces the total run time of the code but also conforms well to the experimental data. Moreover, temperature field at $t = 1$ s and its comparison to the adaptive model are represented in Figure 26. Very good agreement between the uniform and the adaptive model is achieved.

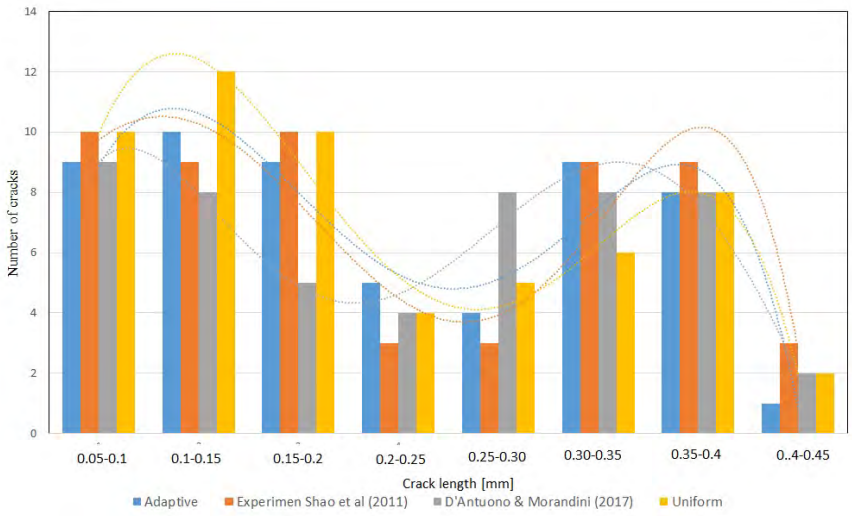

Figure 25: Example III: Crack frequency diagram and interpolation of the results.

Table 2: Comparison of the computational resources used by uniform and refined models in Example III.

	Number of real nodes		
		Adaptive	
	Uniform	Coarse	Fine
$t = 0$ s	24921	6336	0
$t = 1.0$ s		1799	17000
Run time	2016.31 s	817.60 s	

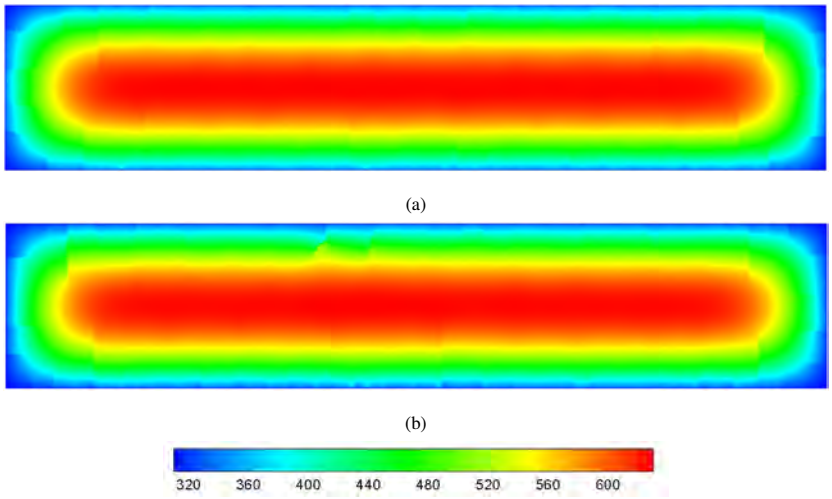

Figure 26: Example III: Temperature ($T[^\circ C]$) after 1.00 s: (a) the adaptive model (b) the uniform model.

5.4. *Example IV: Quenching test of circular ceramic specimen under central thermal shock*

For further validation of the proposed numerical solution, the thermal shock in a circular ceramic plate is investigated. In the experiments done by [6], thin circular ceramic plates are heated to the certain temperature and then dropped into a water bath. These thin plates are stacked together by two thick circular plates on the outside to set the adiabatic condition at the interior surfaces of the thin circular specimens. The circular slab has the radius $R = 0.065\,\mathrm{m}$ as shown in Figure 27. Based on the experimental results in [6], the problem is solved in a plane stress condition with $E = 370 \times 10^9\,\mathrm{Pa}$, $\rho = 3980\,\mathrm{kg/m^3}$, $G_c = 12.16\,\mathrm{J/m^2}$ and $\nu = 1/3$. Furthermore, $m = 3$ is used to solve this example. The convection boundary condition is imposed around the layer of the plate with the thickness of $\bar{\delta}$ as represented in Figure 27. The plate has a temperature-dependent thermal conductivity, specific heat and thermal expansion [65] as shown in Figure 28.

The material of the thin circular ceramic specimens is 99% Al_2O_3. The initial temperature is taken as $\theta_0 = 250\,^\circ\mathrm{C}$ while the temperature of the surfaces contacted with water is $\theta_\infty = 15\,^\circ\mathrm{C}$. This example is solved for a duration of $t = 0.45\,\mathrm{s}$ with a time step of $\Delta t = 10^{-5}\,\mathrm{s}$, which results in 45000 steps.

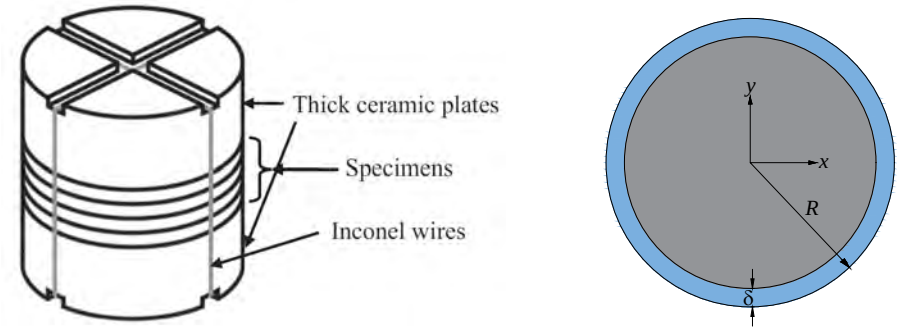

(a) (b)

Figure 27: Geometrical and loading conditions in example IV: (a) schematic diagram [6] and (b) the numerical model [65].

The contour plots of damage obtained by the proposed adaptive model and the uniform model at $t = 0.45$ s are presented in Figure 29. The numerical results illustrate that complex multiple crack paths are initiated from the edge of the circular ceramic specimen and propagate towards the center. Acceptable qualitative and quantitative agreement is obtained between the crack paths of both numerical models and the experimental data. Moreover, the number of total cracks in both simulations as well as the experimental results is 15. Also, the number of long cracks, which their length is more than 50% of the radius of the specimen, is equal to 4 in all models. Additionally, in Table 3, the runtime of each simulation and the number of real nodes are reported. In this example also the total runtime of the simulation is significantly reduced by using the proposed adaptive technique.

Finally, the contour plot of temperature for the adaptive and the uniform models are compared in Figures 30. The comparisons suggest a proper agreement between the models.

6. Conclusions

This paper presents an effective way to use a variable grid size in a weakly coupled thermo-mechanical peridynamic model. The proposed numerical method is equipped with a stretch control criterion to transform the grid discretization adaptively. Hence,

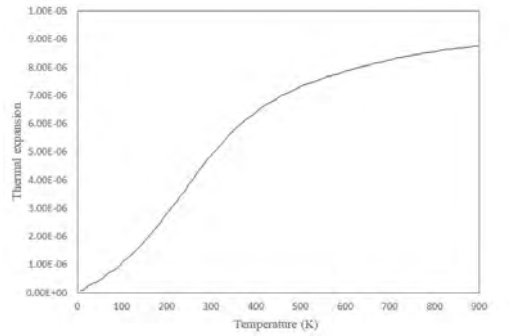

(a)

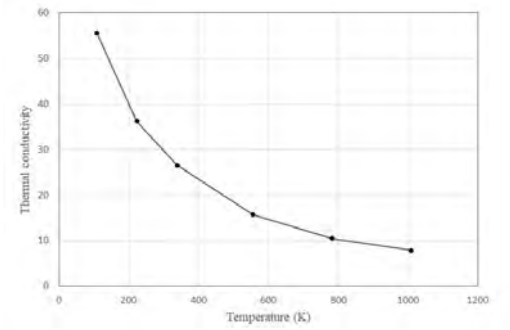

(b)

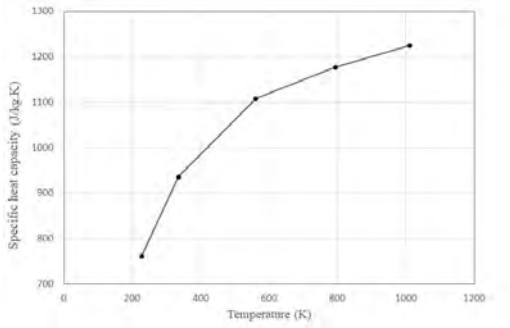

(c)

Figure 28: The temperature-dependent thermal properties of thermal expansion, (b) the thermal conductivity, γ, and the specific heat capacity, c_v in 99% Al_2O_3 ceramics versus temperature [65].

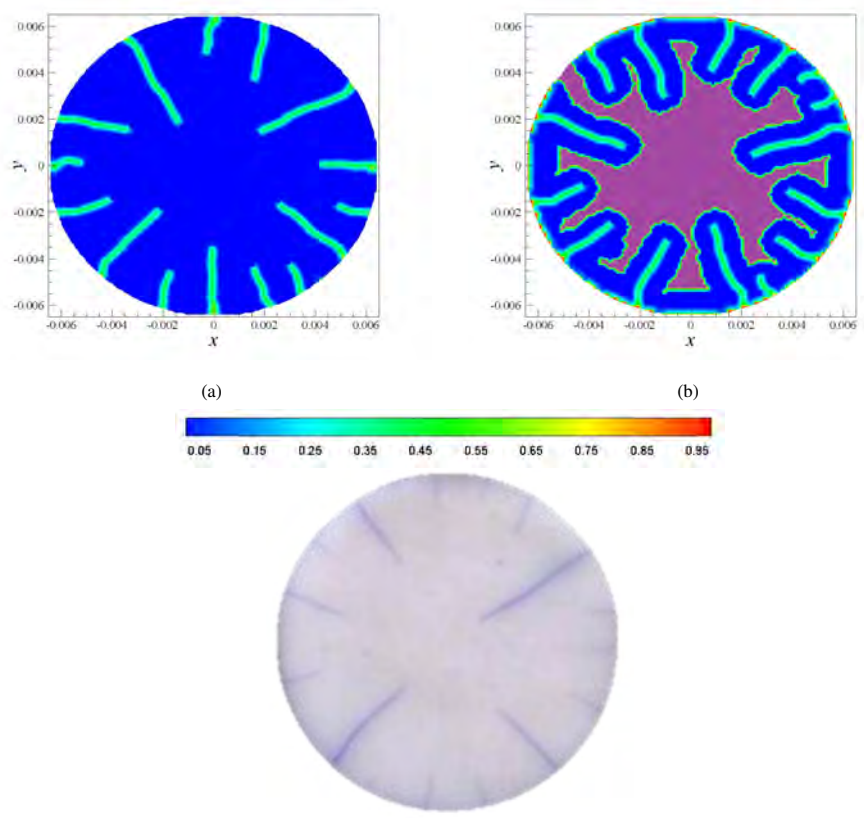

Figure 29: Example III: Damage (ϕ) after 0.45 s: (a) the uniform model (b) the adaptive model (damage only related to the fine grid) (c) experimental model by [6].

Table 3: Comparison of the computational resources used by the uniform model and the adaptive model in Example IV.

	Number of real nodes		
		Adaptive	
	Uniform	Coarse	Fine
$t = 0$ s	17181	4281	0
$t = 0.45$ s		1504	10904
Run time	706.04 s	226.34 s	

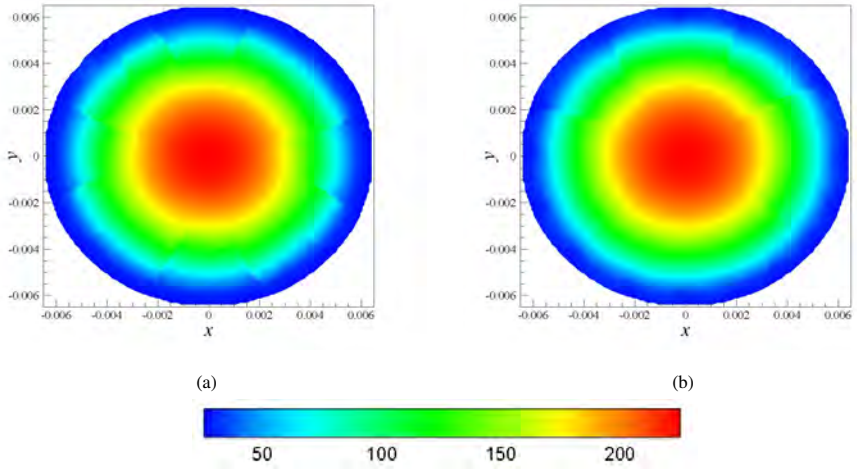

Figure 30: Example IV: Temperature ($T\,°C$) predictions after 0.45 s: (a) the adaptive model (b) the uniform model.

the fine grid spacing is only used in limited zones where it is required. This method is capable of predicting complex crack patterns without any *a priori* hypothesis on crack onset and geometry. By introducing a fine grid discretization over the boundaries of the model, the surface (softening) effect can be reduced significantly. The accuracy and overall performance of the model are examined through problems such as thermo-elastic and thermal-shock induced fracture in ceramics. Results are compared qualitatively and quantitatively to the experimental data, and to numerical solutions produced by standard peridynamic models with uniform grid size and FEM. A remarkable agreement is observed between all sets of results. The new computational method is capable of producing the results of a standard peridynamic model with uniform discretization at a smaller computational cost.

Acknowledgments

The first author acknowledges the financial support of the University of Padova BIRD2017 NR.175705/17.

References

[1] N. P. Padture, M. Gell, E. H. Jordan, Thermal barrier coatings for gas-turbine engine applications, Science 296 (5566) (2002) 280–284. doi:10.1126/science.1068609.

[2] C. P. Jiang, X. F. Wu, J. Li, F. Song, Y. F. Shao, X. H. Xu, P. Yan, A study of the mechanism of formation and numerical simulations of crack patterns in ceramics subjected to thermal shock, Acta Materialia 60 (11) (2012) 4540–4550. doi:https://doi.org/10.1016/j.actamat.2012.05.020.

[3] Y. Shao, Y. Zhang, X. Xu, Z. Zhou, W. Li, B. Liu, Z. Jin, Effect of crack pattern on the residual strength of ceramics after quenching, Journal of the American Ceramic Society 94 (9) (2011) 2804–2807. doi:doi:10.1111/j.1551-2916.2011.04728.x.

[4] S. Honda, Y. Ogihara, T. Kishi, S. Hashimoto, Y. Iwamoto, Estimation of thermal shock resistance of fine porous alumina by infrared radiation heating method, Journal of the Ceramic Society of Japan 117 (1371) (2009) 1208–1215. doi:10.2109/jcersj2.117.1208.

[5] S. Honda, T. Suzuki, T. Nishikawa, H. Awaji, Y. Akimune, N. Hirosaki, Estimation of thermal shock properties for silicon nitride having high thermal conductivity, Journal of the Ceramic Society of Japan 110 (1277) (2002) 38–43. doi:10.2109/jcersj.110.38.

[6] Y. Liu, X. Wu, Q. Guo, C. Jiang, F. Song, J. Li, Experiments and numerical simulations of thermal shock crack patterns in thin circular ceramic specimens, Ceramics International 41 (1, Part B) (2015) 1107–1114. doi:https://doi.org/10.1016/j.ceramint.2014.09.036.

[7] Z. P. Bažant, H. Ohtsubo, K. Aoh, Stability and post-critical growth of a system of cooling or shrinkage cracks, International Journal of Fracture 15 (5) (1979) 443–456. doi:10.1007/bf00023331.

[8] S. Nemat-Nasser, Stability of a system of interacting cracks, International Journal of Engineering Science 16 (4) (1978) 277–285. doi:https://doi.org/10.1016/0020-7225(78)90094-0.

[9] D. P. H. Hasselman, Elastic energy at fracture and surface energy as design criteria for thermal shock, Journal of the American Ceramic Society 46 (11) (1963) 535–540. doi:doi:10.1111/j.1151-2916.1963.tb14605.x.

[10] W. D. Kingery, Factors affecting thermal stress resistance of ceramic materials, Journal of the American Ceramic Society 38 (1) (1955) 3–15. doi:doi:10.1111/j.1151-2916.1955.tb14545.x.

[11] D. P. H. Hasselman, Unified theory of thermal shock fracture initiation and crack propagation in brittle ceramics, Journal of the American Ceramic Society 52 (11) (1969) 600–604. doi:doi:10.1111/j.1151-2916.1969.tb15848.x.

[12] G. A. Schneider, Thermal shock criteria for ceramics, Ceramics International 17 (6) (1991) 325–333. doi:https://doi.org/10.1016/0272-8842(91)90029-Y.

[13] H. A. Bahr, H. J. Weiss, H. G. Maschke, F. Meissner, Multiple crack propagation in a strip caused by thermal shock, Theoretical and Applied Fracture Mechanics 10 (3) (1988) 219–226. doi:https://doi.org/10.1016/0167-8442(88)90014-6.

[14] S. Tarasovs, A. Ghassemi, Self-similarity and scaling of thermal shock fractures, Physical Review E 90 (1) (2014) 012403. doi:10.1103/PhysRevE.90.012403.

[15] T. Menouillard, T. Belytschko, Analysis and computations of oscillating crack propagation in a heated strip, International Journal of Fracture 167 (1) (2011) 57–70. doi:10.1007/s10704-010-9519-0.

[16] M. M. Rokhi, M. Shariati, Implementation of the extended finite element method for coupled dynamic thermoelastic fracture of a functionally graded cracked layer, Journal of the Brazilian Society of Mechanical Sciences and Engineering 35 (2) (2013) 69–81. doi:10.1007/s40430-013-0015-0.

[17] A. Zamani, M. R. Eslami, Implementation of the extended finite element method for dynamic thermoelastic fracture initiation, International Journal of Solids and Structures 47 (10) (2010) 1392–1404. doi:https://doi.org/10.1016/j.ijsolstr.2010.01.024.

[18] B. Bourdin, J.-J. Marigo, C. Maurini, P. Sicsic, Morphogenesis and propagation of complex cracks induced by thermal shocks, Physical Review Letters 112 (1) (2014) 014301. doi:10.1103/PhysRevLett.112.014301.

[19] D. Chu, X. Li, Z. Liu, Study the dynamic crack path in brittle material under thermal shock loading by phase field modeling, International Journal of Fracture 208 (1) (2017) 115–130. doi:10.1007/s10704-017-0220-4.

[20] S. B. Tang, H. Zhang, C. A. Tang, H. Y. Liu, Numerical model for the cracking behavior of heterogeneous brittle solids subjected to thermal shock, International

Journal of Solids and Structures 80 (2016) 520–531. doi:https://doi.org/10.1016/j.ijsolstr.2015.10.012.

[21] J. Li, F. Song, C. Jiang, A non-local approach to crack process modeling in ceramic materials subjected to thermal shock, Engineering Fracture Mechanics 133 (2015) 85–98. doi:https://doi.org/10.1016/j.engfracmech.2014.11.007.

[22] S. A. Silling, Reformulation of elasticity theory for discontinuities and long-range forces, Journal of the Mechanics and Physics of Solids 48 (1) (2000) 175–209. doi:https://doi.org/10.1016/S0022-5096(99)00029-0.

[23] S. A. Silling, M. Epton, O. Weckner, J. Xu, E. Askari, Peridynamic states and constitutive modeling, Journal of Elasticity 88 (2) (2007) 151–184. doi:10.1007/s10659-007-9125-1.

[24] Y.-T. Wang, X.-P. Zhou, M.-M. Kou, Three-dimensional numerical study on the failure characteristics of intermittent fissures under compressive-shear loads, Acta Geotechnica 14 (4) (2019) 1161–1193.

[25] S. Bazazzadeh, A. Shojaei, M. Zaccariotto, U. Galvanetto, Application of the peridynamic differential operator to the solution of sloshing problems in tanks, Engineering Computations 36 (1) (2018) 45–83.

[26] S. Bazazzadeh, M. Zaccariotto, U. Galvanetto, Fatigue degradation strategies to simulate crack propagation using peridynamic based computational methods, Latin American Journal of Solids and Structures 16 (2) (2019).

[27] M. Zaccariotto, G. Sarego, D. Dipasquale, A. Shojaei, S. Bazazzadeh, T. Mudric, M. Duzzi, U. Galvanetto, Discontinuous mechanical problems studied with a peridynamics-based approach, Aerotecnica Missili & Spazio 96 (1) (2017) 44–55. doi:10.1007/BF03404736.
URL https://doi.org/10.1007/BF03404736

[28] A. Shojaei, U. Galvanetto, T. Rabczuk, A. Jenabi, M. Zaccariotto, A generalized finite difference method based on the peridynamic differential operator for the

solution of problems in bounded and unbounded domains, Computer Methods in Applied Mechanics and Engineering 343 (2019) 100–126.

[29] B. Kilic, E. Madenci, Prediction of crack paths in a quenched glass plate by using peridynamic theory, International Journal of Fracture 156 (2) (2009) 165–177. doi:10.1007/s10704-009-9355-2.

[30] Z. Xu, G. Zhang, Z. Chen, F. Bobaru, Elastic vortices and thermally-driven cracks in brittle materials with peridynamics, International Journal of Fracture 209 (1) (2018) 203–222. doi:10.1007/s10704-017-0256-5.

[31] W. Gerstle, N. Sau, S. Silling, Peridynamic modeling of concrete structures, Nuclear Engineering and Design 237 (12) (2007) 1250–1258. doi:https://doi.org/10.1016/j.nucengdes.2006.10.002.

[32] F. Bobaru, M. Duangpanya, The peridynamic formulation for transient heat conduction, International Journal of Heat and Mass Transfer 53 (19) (2010) 4047–4059. doi:https://doi.org/10.1016/j.ijheatmasstransfer.2010.05.024.

[33] F. Bobaru, M. Duangpanya, A peridynamic formulation for transient heat conduction in bodies with evolving discontinuities, Journal of Computational Physics 231 (7) (2012) 2764–2785. doi:https://doi.org/10.1016/j.jcp.2011.12.017.

[34] S. Oterkus, E. Madenci, A. Agwai, Peridynamic thermal diffusion, Journal of Computational Physics 265 (2014) 71–96.

[35] A. G. Agwai, A peridynamic approach for coupled fields, Thesis (2011).

[36] S. Oterkus, E. Madenci, A. Agwai, Fully coupled peridynamic thermomechanics, Journal of the Mechanics and Physics of Solids 64 (2014) 1–23. doi:https://doi.org/10.1016/j.jmps.2013.10.011.

[37] S. Oterkus, E. Madenci, Peridynamic modeling of fuel pellet cracking, Engineering Fracture Mechanics 176 (2017) 23–37. doi:https://doi.org/10.1016/j.engfracmech.2017.02.014.

[38] P. D'Antuono, M. Morandini, Thermal shock response via weakly coupled peridynamic thermo-mechanics, International Journal of Solids and Structures 129 (2017) 74–89. doi:https://doi.org/10.1016/j.ijsolstr.2017.09.010.

[39] Y. Wang, X. Zhou, M. Kou, A coupled thermo-mechanical bond-based peridynamics for simulating thermal cracking in rocks, International Journal of Fracture 211 (1) (2018) 13–42. doi:10.1007/s10704-018-0273-z.

[40] Y. Wang, X. Zhou, M. Kou, Peridynamic investigation on thermal fracturing behavior of ceramic nuclear fuel pellets under power cycles, Ceramics International 44 (10) (2018) 11512–11542. doi:https://doi.org/10.1016/j.ceramint.2018.03.214.

[41] Y.-T. Wang, X.-P. Zhou, Peridynamic simulation of thermal failure behaviors in rocks subjected to heating from boreholes, International Journal of Rock Mechanics and Mining Sciences 117 (2019) 31–48.

[42] Y. Wang, X. Zhou, T. Zhang, Size effect of thermal shock crack patterns in ceramics: Insights from a nonlocal numerical approach, Mechanics of Materials 137 (2019) 103–133.

[43] X. Gu, Q. Zhang, X. Xia, Voronoi-based peridynamics and cracking analysis with adaptive refinement, International Journal for Numerical Methods in Engineering 112 (13) (2017) 2087–2109. doi:10.1002/nme.5596.

[44] P. Seleson, S. Beneddine, S. Prudhomme, A force-based coupling scheme for peridynamics and classical elasticity, Computational Materials Science 66 (2013) 34–49. doi:https://doi.org/10.1016/j.commatsci.2012.05.016.

[45] A. Shojaei, T. Mudric, M. Zaccariotto, U. Galvanetto, A coupled meshless finite point/peridynamic method for 2d dynamic fracture analysis, International Journal of Mechanical Sciences 119 (2016) 419–431. doi:https://doi.org/10.1016/j.ijmecsci.2016.11.003.

[46] A. Shojaei, M. Zaccariotto, U. Galvanetto, Coupling of 2d discretized peridynamics with a meshless method based on classical elasticity using switching of nodal behaviour, Engineering Computations 34 (5) (2017) 1334–1366.

[47] M. Zaccariotto, T. Mudric, D. Tomasi, A. Shojaei, U. Galvanetto, Coupling of fem meshes with peridynamic grids, Computer Methods in Applied Mechanics and Engineering 330 (2018) 471–497. doi:https://doi.org/10.1016/j.cma.2017.11.011.

[48] H. Ren, X. Zhuang, Y. Cai, T. Rabczuk, Dual-horizon peridynamics, International Journal for Numerical Methods in Engineering 108 (12) (2016) 1451–1476. doi:10.1002/nme.5257.

[49] A. Shojaei, F. Mossaiby, M. Zaccariotto, U. Galvanetto, An adaptive multi-grid peridynamic method for dynamic fracture analysis, International Journal of Mechanical Sciences 144 (2018) 600–617.

[50] F. Mossaiby, A. Shojaei, M. Zaccariotto, U. Galvanetto, Opencl implementation of a high performance 3d peridynamic model on graphics accelerators, Computers and Mathematics with Applications 74 (8) (2017) 1856–1870. doi:https://doi.org/10.1016/j.camwa.2017.06.045.

[51] E. Emmrich, O. Weckner, The peridynamic equation and its spatial discretisation, Mathematical Modelling and Analysis 12 (1) (2007) 17–27. doi:10.3846/1392-6292.2007.12.17-27.

[52] S. A. Silling, E. Askari, A meshfree method based on the peridynamic model of solid mechanics, Computers and Structures 83 (17) (2005) 1526–1535. doi:https://doi.org/10.1016/j.compstruc.2004.11.026.

[53] Y. D. Ha, F. Bobaru, Studies of dynamic crack propagation and crack branching with peridynamics, International Journal of Fracture 162 (1) (2010) 229–244. doi:10.1007/s10704-010-9442-4.

[54] K. Yu, X. J. Xin, K. B. Lease, A new adaptive integration method for the peridynamic theory, Modelling and Simulation in Materials Science and Engineering 19 (4) (2011) 045003.

[55] W. H. Gerstle, Introduction to practical peridynamics: computational solid mechanics without stress and strain, Vol. 1, World Scientific Publishing Company, 2015.

[56] S. Nikravesh, W. Gerstle, Improved state-based peridynamic lattice model including elasticity, plasticity and damage, CMES-Comput Model Eng 116 (3) (2018) 323–347.

[57] A. S. Day, An introduction to dynamic relaxation, The Engineering 219 (5688) (1965) 218–221.

[58] D. Huang, G. Lu, P. Qiao, An improved peridynamic approach for quasi-static elastic deformation and brittle fracture analysis, International Journal of Mechanical Sciences 94-95 (2015) 111–122. doi:https://doi.org/10.1016/j.ijmecsci.2015.02.018.

[59] B. Kilic, E. Madenci, An adaptive dynamic relaxation method for quasi-static simulations using the peridynamic theory, Theoretical and Applied Fracture Mechanics 53 (3) (2010) 194–204. doi:https://doi.org/10.1016/j.tafmec.2010.08.001.

[60] S. Oterkus, Peridynamics for the solution of multiphysics problems, Thesis (2015).

[61] H. Awaji, S. Honda, N. Yamamoto, T. Endo, N. Hirosaki, Thermal Shock Strength and Thermal Shock Fracture Toughness of Ceramics, Springer US, Boston, MA, 2002, pp. 363–379. doi:https://doi.org/10.1007/978-1-4757-4019-6_29.

[62] D. R. Jenkins, Optimal spacing and penetration of cracks in a shrinking slab, Physical Review E 71 (5) (2005) 056117. doi:10.1103/PhysRevE.71.056117.

[63] I. N. Giannakeas, T. K. Papathanasiou, H. Bahai, Simulation of thermal shock cracking in ceramics using bond-based peridynamics and fem, Journal of the European Ceramic Society 38 (8) (2018) 3037–3048. doi:https://doi.org/10.1016/j.jeurceramsoc.2017.12.039.

[64] Y. Wang, X. Zhou, M. Kou, Numerical studies on thermal shock crack branching instability in brittle solids, Engineering Fracture Mechanics 204 (2018) 157 – 184. doi:https://doi.org/10.1016/j.engfracmech.2018.08.028.
URL http://www.sciencedirect.com/science/article/pii/S0013794418303990

[65] Y. Wang, X. Zhou, M. Kou, An improved coupled thermo-mechanic bond-based peridynamic model for cracking behaviors in brittle solids subjected to thermal shocks, European Journal of Mechanics - A/Solids 73 (2019) 282 – 305. doi:https://doi.org/10.1016/j.euromechsol.2018.09.007.

Conflict of Interest and Authorship Conformation Form

Please check the following as appropriate:

- ✓ All authors have participated in (a) conception and design, or analysis and interpretation of the data; (b) drafting the article or revising it critically for important intellectual content; and (c) approval of the final version.
- ✓ This manuscript has not been submitted to, nor is under review at, another journal or other publishing venue.
- ✓ The authors have no affiliation with any organization with a direct or indirect financial interest in the subject matter discussed in the manuscript
- ✓ The following authors have affiliations with organizations with direct or indirect financial interest in the subject matter discussed in the manuscript:

Author's name	Affiliation
Soheil Bazazzadeh	Industrial Engineering Department, University of Padova, v. Venezia 1, Padova 35131, Italy" and "Center of Studies and Activities for Space (CISAS)-"G. Colombo", v. Venezia 15, Padova 35131, Italy
Farshid Mossaiby	Department of Civil Engineering, University of Isfahan, 81744-73441 Isfahan, Iran
Arman Shojaei	Institute of Materials Research, Materials Mechanics, Helmholtz-Zentrum Geesthacht, Max-Planck-Strasse 1, 21502, Geesthacht, Germany